GEOMETRY GENERATION FOR COMPUTER AIDED ENGINEERING.

STUDY CASES IN MESHING AND CERAMICS MODELING.

GEOMETRY GENERATION FOR COMPUTER AIDED ENGINEERING. STUDY CASES IN MESHING AND CERAMICS MODELING.

Ricardo Serrano Salazar

Advisor: Oscar E. Ruiz

Submitted in partial fulfillment of the requirements for the degree of Bachelor of Science in Systems Engineering.

Department of Computer Science
EAFIT University
April 2009

Contents

List of Figures

List of Tables

Introduction

Computational modeling is the use of algorithms and data structures to transform a physical or theoretical problem into a problem solvable by a computer. The branch of Computer Science that supports engineers in tasks like analysis, simulation, design, manufacture, planning, diagnosis and repair is the Computer Aided Engineering (CAE). Some of the problems found in CAE, like the ones described in this thesis, require extensive use of Geometric Modeling. Geometric Modeling is the branch of Applied Mathematics and Computational Geometry that studies methods and algorithms for the mathematical description of shapes.

Several engineering problems depend on too complicated equations to be solved analytically. One of the methods developed for solving partial differential, (and other kind of), equations is the Finite Element Method (FEM). FEM decomposes a problem into simpler sub-domains and feeds it to a solver, which gives a solution.

Modeling a problem by means of the FEM broadly consists of:

1. Modeling the geometry.
2. Meshing (Discretization).
3. Specification of material property.
4. Specification of boundary, initial and loading conditions.

At the CAD/CAM/CAE laboratory EAFIT and at the CITG UPV two different projects were carried on. One aimed to produce a mesher of a parametric surface that could be used for FEM. The second one tried to model, using commercial FEM packages, the stages that the ceramic tile undergoes during its production. The results of both projects are presented in the manner of papers with the following titles:

1. Gabriel-constrained Parametric Surface Triangulation.
2. Simulation of the handling in green of ceramic tiles with deep back relief.

The topic of the first paper is the triangulation of a parametric surface $S : \mathbb{R}^2 \longrightarrow \mathbb{R}^3$, of the class C^2 with border. The boundary of S is the collection of loops L_i embedded in S. The triangulation algorithm generates a mesh that is also a 2-manifold but of the class C^0 with border. The algorithm receives as an input a boundary representation model (b-rep): one of the most common ways in which CAD systems model the geometry and topology of solids.

The chapter presents:

1. A literature review of algorithms that triangulate surfaces. Most of these algorithms don't have any guarantee or special method to handle the border properly.
2. An introduction to the Gabriel Complex. Also, an introduction to the curvature of smooth parametric surfaces.
3. Four algorithms that take care of each stage of the triangulation of a (b-rep).
4. The complexities of each of the algorithms.
5. Results, conclusions and future work.

The topic of the second paper is the use of the FEM for the evaluation of the handling in green of a ceramic tile. The ceramic tile evaluated has deep back relief. Tiles with back relief can have different mechanical behavior than their counterparts. A ceramic tile is said to be in green state after pressure forming. It has a high content of water and it's in its weakest state; because of this, the tile in this stage does not undergo many processes. An evaluation of the strength for the different processes that the tile undergoes during this stage can be done with help of the FEM. To be able to do this with a parametric approach, a computer software that received a set of parameters to generate the model of tile with back relief was created. It applied the necessary boundary conditions and the rest of the steps needed to use FEM so the model would be ready to be solved. It also generated a set of commands that were fed to ANSYS®, which performed a set of boolean operations that gave as result the geometric model of the tile required.

The chapter presents:

1. A description of the steps taken by a user in ANSYS® to model a problem by means of the FEM and how we improved that workflow for the specific problem of modeling the production stages that a ceramic tile with deep back relief undergoes.
2. An introduction to theories needed to model the problem by means of the FEM.
3. An evaluation of the strength of tiles lightened by a method simpler than the back relief: reducing their thickness.
4. An evaluation of the strength of tiles with a model of back relief but with different parameters.

5. A method to evaluate the appropriateness of a back relief for any given test.
6. Conclusions and future work.

Chapter 1

Gabriel-constrained Parametric Surface Triangulation

Context

The CAD/CAM/CAE Laboratory at EAFIT University, under my coordination, started in 2007 the project: *Stochastical Computational Geometry in CAD CAM CAE*. As part of this project, some probably correct sampling and reconstruction algorithms have been proposed and developed by me, the Professors and the assistants at the lab. One of such projects involved Ricardo Serrano who implemented an algorithm that triangulates b-reps.

The algorithms developed used knowledge in the fields of Theoretical and Computational Geometry, Computer Assisted Design, Geometric Modeling, Graph Theory and Software Development in the C++ language. This research has great application in the field of Computer Aided Engineering, specifically the FEM, and in the field of Computer Aided Manufacturing.

The theoretical contributions of the project appear on the paper:

1. Oscar E. Ruiz, Carlos Cadavid, Juan G. Lalinde, Ricardo Serrano, and Guillermo Peris-Fajarnes. Gabriel-constrained parametric surface triangulation. Proceedings of World Academy of Science, Engineering, and Technolgy, 34:578 585, 2008.
2. Oscar E. Ruiz, John Congote, Carlos Cadavid, Juan G. Lalinde, Guillermo Peris-Fajarnés, Beatriz Defez, Ricardo Serrano. Gabriel-constrained, parameter-independent, curvature-sensitive parametric surface triangulations. Advanced Technologies, ISBN 978-953-7619-X-X.

As coauthor of the publications we give the permissions for this material to appear in this document. We are ready to provide any additional information on the subject, as needed.

Prof. Dr. Eng. Oscar E. Ruiz
oruiz@eafit.edu.co
Coordinator CAD CAM CAE Laboratory
EAFIT University
Medellín, Colombia

Abstract

The Boundary Representation of a 3D manifold contains FACES (connected subsets of a parametric surface $S : \mathbb{R}^2 \longrightarrow \mathbb{R}^3$). In many science and engineering applications it is cumbersome and algebraically difficult to deal with the polynomial set and constraints (LOOPs) representing the FACE. Because of this reason, a Piecewise Linear (PL) approximation of the FACE is needed, which is usually represented in terms of triangles (i.e. 2-simplices). Solving the problem of FACE triangulation requires producing quality triangles which are: (i) independent of the arguments of S, (ii) sensitive to the local curvatures, and (iii) compliant with the boundaries of the FACE and (iv) topologically compatible with the triangles of the neighboring FACEs. In the existing literature there are no guarantees for the point (iii). This article contributes to the topic of triangulations conforming to the boundaries of the FACE by applying the concept of parameter-independent Gabriel complex, which improves the correctness of the triangulation regarding aspects (iii) and (iv). In addition, the article applies the geometric concept of tangent ball to a surface at a point to address points (i) and (ii). Additional research is needed in algorithms that (i) take advantage of the concepts presented in the heuristic algorithm proposed and (ii) can be proved correct.

Glossary

S:	Parametric Surface. $S : \mathbb{R}^2 \rightarrow \mathbb{R}^3$. is an (infinite) 2-manifold without border.
F,H:	Faces. Connected subsets of a parametric surface ($F, H \subset S$).
$S^{-1}(F)$:	Pre-image of F in parametric space $U - V$.
T_F:	Triangulation of face F in Euclidean space.
T_{UV}:	A triangulation in parametric space $U - V$.
$T = S(T_{UV})$:	Triangulation in $\mathbb{R}^3$ as a mapping, via S, of the triangulation T_{UV} in $U - V$ parametric space.
∂X:	Boundary of the set X.
L_i:	A loop ($L_i \subseteq \partial F$), is a 1-manifold without border. It is a connected subset of the boundary of F.
E_j	An edge ($E_j \subseteq L_i$), is a 1-manifold with border.
t:	A triangle of the triangulation T.
p, q:	Points in Euclidean space. $p, q \in \mathbb{R}^3$.
u, v, w:	Real parameters of a curve $C(w)$ or a surface $S(u, v)$.
$cl(A)$:	Closure of the set A. $cl(A) = A \cup \partial A$.
$int(A)$:	Interior of the set A. $int(A) = A - \partial A$.
$B_G(p, q, r)$:	Gabriel Ball in $\mathbb{R}^3$. Spherical point set whose center is contained in the plane pqr, passing through the points $p, q, r \in R^3$.
$B_G(p, q)$:	Gabriel Ball in $\mathbb{R}^3$. Spherical point set whose center is contained in the edge pq, passing through the points $p, q \in \mathbb{R}^3$.
e:	Edge of a triangle.

1.1 Introduction

Boundary Representations, B-Reps, are the computer formalization of the boundary of a body ($M = \partial BODY$). Shortly, M is a collection of SHELLs, which in turn are collections of FACEs. For convenience, we will assume that the SHELLs are 2-manifolds without border in $\mathbb{R}^3$. Each SHELL is decomposed into FACEs, which must have boundary. It is customary in geometric modeling to make a FACE F a connected proper subset of *one* parametric surface $S(u, v) \subset \mathbb{R}^3$. In this article we consider the b-reps as closed 2-manifolds with continuity C^2 inside each face and C^0 among them.

The border of F is ∂F, which is the collection of LOOPs L_i embedded in S. The LOOP L_i can be thought of as a 1-manifold without border, with C^∞ continuity except in a finite number of points, where it is C^0-continuous. In such locations L_i is split into EDGEs E_j, each one being a C^∞ 1-manifold with border. The problem of surface triangulation takes place in one of such FACEs F. A PL approximation T_F of face F is required which: (a) is formed by triangles, (b) departs from F in less than a distance ϵ, (c) has triangles as equilateral as possible, (d) has as few triangles as possible, and, (e) each edge e_j of the triangle set has exactly two incident triangles. Property (e) is a consequence of the fact that a B-Rep is a 2-manifold without boundary. The triangulation T is also a 2-manifold (of the C^0 class) without boundary. Condition (e) also holds for edges e_j whose extremes lie on any loop L_i. This means, this edge e_i receives a triangle from the triangulation T_F (face F) and another from the triangulation T_H (face H).

An important aspect to control in triangulating a face F is that having a triangulation T_{UV} correctly covering $S^{-1}(F)$ in parametric space $U-V$ is not a guarantee for the triangulation $T = S(T_{UV})$ in $\mathbb{R}^3$ to be correct. Several problems may arise: (i) Fig. 1.1 illustrates that a completely internal triangle $[a, b, c]$ in parametric space $U-V$ may not be mapped by S to an internal triangle $[S(a), S(b), S(c)]$ in $\mathbb{R}^3$. (ii) roughly equilateral triangles t in $U-V$ space may map to extremely deformed triangles $S(t)$ in $\mathbb{R}^3$ because of sharp warping caused by S, (iii) neighboring triangles $t_i, t_j, t_k, ...$ in $U-V$ space mapped via $S()$ may form a fish scale effect in R^3 because of the same warping in S.

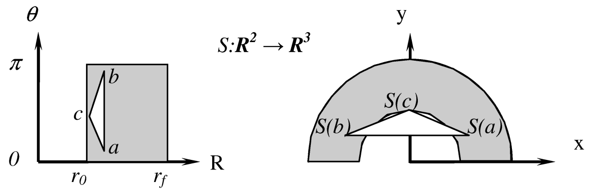

Figure 1.1: Triangle abc is internal in parameter space. Triangle $S(a)S(b)S(c)$ is external to the surface $S(r, \theta) = (r\cos(\theta), r\sin(\theta), 0)$

1.2 Related Work

1.2.1 Fundamental definitions

As discussed in [1] a smooth 2-manifold with boundary (face) F is a sub-manifold of a smooth 2-manifold S without boundary. If the neighborhood of a point $p \in F$ is homeomorphic to a 2 dimensional euclidean space, then we say that the p is in the interior of F ($int(F)$). If the neighborhood of a point p in F is homeomorphic to a half euclidean space then we say that the point is in the boundary of F (∂F). The exterior of the submanifold F is composed by the points $p \in S$ and not in the closure of F

($p \notin cl(F)$). It includes all the points neither in the interior nor the boundary of F but still in S. The boundary is a closed set and the interior and exterior are open sets. In Fig. 1.4 the interior, boundary and exterior are shown ($A - B$ denotes the difference between sets A and B).

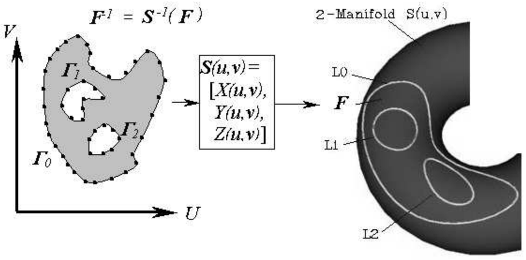

Figure 1.2: Pre-image $F^{-1} = S^{-1}(F)$ of the face F by the parametric surface S.

Fig. 1.2 displays the general situation in which a face F is carried by a parametric surface S in $\mathbb{R}^3$. F is a connected subset of S, with the boundary of F, $\partial F = \{L_0, ..., L_n\}$ being the set of loops L_i which limit F on S. If the function $S(u, v)$ is 1-1 (which can be guaranteed by a convenient decomposition of the overall B-Rep) then there exists a pre-image of F in parametric space $U \times V$, that we call F^{-1}. Such a region can be calculated as $F^{-1} = S^{-1}(F)$. To do so, a point sample of ∂F formed by points $p_i \in \mathbb{R}^3$ is tracked back to their pre-images $(u_i, v_i) \in (U \times V)$ therefore rendering a connected region $F^{-1} \subset (U \times V)$, most likely with holes, bounded by a set of planar Jordan curves $\partial F^{-1} = \{\Gamma_0, ..., \Gamma_n\}$.

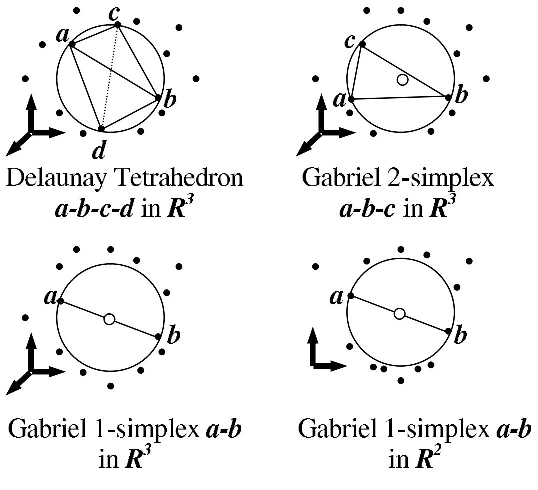

Delaunay Tetrahedron ***a-b-c-d*** in $\boldsymbol{R^3}$

Gabriel 2-simplex ***a-b-c*** in $\boldsymbol{R^3}$

Gabriel 1-simplex ***a-b*** in $\boldsymbol{R^3}$

Gabriel 1-simplex ***a-b*** in $\boldsymbol{R^2}$

Figure 1.3: Delaunay tetrahedron for points $a, b, c, d \in \mathbb{R}^3$, Gabriel 2-simplex for $a, b, c \in \mathbb{R}^3$, Gabriel 1-simplex for $a, b \in \mathbb{R}^3$, Gabriel 1-simplex for $a, b \in \mathbb{R}^2$.

Fig. 1.3 displays a short collection of Delaunay and Gabriel complexes. A Delaunay tetrahedron in a set of points in 3D is a tetrahedron (3-simplex) formed by four points whose circumscribed sphere contains no other point of the set. Given vertices $v_i v_j v_k$ in the point set, they form a Gabriel triangle (2-simplex) if the smallest sphere through them contains no other point of the set. The triangle $v_i v_j v_k$ is embedded in the equatorial plane of such a sphere. A Gabriel edge $v_i v_j$ (1-simplex) is one with v_i and v_j in the point set, such that the sphere centered in $(v_i + v_j)/2$ with radius $r = d(v_i, v_j)/2$ contains no point of the sample other than v_i and v_j. Such a sphere is the smallest one containing v_i and v_j. Each Gabriel 1-simplex makes part of at least one Gabriel 2-simplex, and each Gabriel 2-simplex makes part of at least one Delaunay tetrahedra.

The present article applies the Gabriel variant (1- and 2- simplices) to Delaunay connectivity to calculate a triangulation for a point sample V_F (sensitive to curvature and independent of the parameterization) on the face F, carried by a parametric surface S. Section 2 reviews theoretical and algorithmic knowledge related to triangulations and surface curvatures. Section 3 discusses the algorithms devised and implemented to triangulate Boundary Representations. Section 4 presents five complex Boundary Representations with manufacturing and organic surfaces and high genii triangulated by the implemented algorithm. Section 5 concludes this article and sketches directions for future work.

1.2.2 Curvature Measurement in Parametric Surfaces

A parametric surface is a function $S : \mathbb{R}^2 \rightarrow \mathbb{R}^3$, which we assume to be twice derivable in every point. The derivatives are named in the following manner ([10], [20],):

$$S_u = \frac{\partial S}{\partial u};\ S_v = \frac{\partial S}{\partial v};\ S_{uu} = \frac{\partial^2 S}{\partial u^2};\ S_{vv} = \frac{\partial^2 S}{\partial v^2}; \qquad (1.2.1)$$
$$S_{uv} = S_{vu} = \frac{\partial^2 S}{\partial u \partial v};\ n = \frac{S_u \times S_v}{|S_u \times S_v|}$$

with n being the unit vector normal to the surface S at $S(u, v)$.

The Gaussian and Mean curvatures are given by:

$$K = \frac{LN - MM}{EG - FF}; H = \frac{LG - 2MF + NE}{2(EG - FF)}; \qquad (1.2.2)$$

where the coefficients E, F, G, L, M, N are:

$$E = S_u \bullet S_u; \quad F = S_u \bullet S_v = S_v \bullet S_u; \qquad (1.2.3)$$
$$G = S_v \bullet S_v; \quad L = S_{uu} \bullet n;$$
$$M = S_{uv} \bullet n; \quad N = S_{vv} \bullet n;$$

Minimal, Maximal, Gaussian, Mean Curvatures from the Weingarten Application The Weingarten Application ([10]), W is an alternative way to calculate the Gaussian and Mean curvatures.

$$W = \begin{bmatrix} a_{11} & a_{12} \\ a_{21} & a_{22} \end{bmatrix} \tag{1.2.4}$$

with $a_{11}, a_{12}, a_{21}, a_{22}$ being:

$$\begin{aligned} a_{11} &= \frac{MF - LG}{EG - F^2}; \quad a_{12} = \frac{NF - MG}{EG - F^2}; \\ a_{21} &= \frac{LF - ME}{EG - F^2}; \quad a_{22} = \frac{MF - NE}{EG - F^2} \end{aligned} \tag{1.2.5}$$

The following facts allow to calculate the curvature measures for S from the Weingarten Application: (i) The eigenvalues k_1 y k_2 of W are called **Principal Curvatures**, with k_1 being the *maximal* curvature and k_2 being the *minimal* curvature (assume that $|k_1| \geq |k_2|$). (ii) $K = det(W)$ is the **Gaussian Curvature**, with $K = k_1 * k_2$. (iii) $2H = trace(W)$ is twice the **Mean Curvature**, with $H = \frac{k_1+k_2}{2}$. (iv) The maximal and minimal curvatures are: $k_1 = H + \sqrt{H^2 - K}$ and $k_2 = H - \sqrt{H^2 - K}$.

$W * v = k * v$ is the eigenpair equation for the W matrix. The solutions for such an equation are the eigenpairs (k_1, v_1) and (k_2, v_2). Therefore, $W * v_1 = k_1 * v_1$ and $W * v_2 = k_2 * v_2$. The directions of principal curvature *in $U \times V$ space* are v_1 and v_2 ($v_1 = (w_{11}, w_{12})$ and $v_2 = (w_{21}, w_{22})$). The directions of maximal and minimal curvatures in R^3 are $u_1 = w_{11} * S_u + w_{12} * S_v$ and $u_2 = w_{21} * S_u + w_{22} * S_v$, respectively.

1.2.3 Previous Work

[12] implements an algorithm which starts with an already valid triangulation on a trimmed surface $S(u, v)$ and originates a new triangular mesh. It proposes a surface triangulation with a Delaunay method given 3 points in $\mathbb{R}^3$ which determine a sphere whose equatorial plane is defined by the 3 given points. The algorithm creates a point set which may be more dense as needed by a particular criterion (e.g. curvature). This algorithm uses expensive operations (e.g. surface-line intersection). The boundary of the triangulated trimmed and meshed face is expressed and calculated in handled in parametric space. Since the algorithm in [12] starts with a given triangulation and modifies it, if such triangulation is not correct, or it does not respect the boundary of the trimmed surface, the triangulations following keep such characteristic. According to [16], the restricted Delaunay triangulation of general topological spaces is defined. The restricted Delaunay triangulation in the case of trimmed surface in $\mathbb{R}^3$ is the dual of the Voronoi diagram intersected with the surface. Therefore, a triangle is created in each intersection of 3 voronoi cells with the surface. A contribution of the paper is to show that Chew's algorithm is a restricted Delaunay triangulation.

In the problem of the triangulation of manifolds with boundary the theoretical guaranties that serve for surface reconstruction do not apply. For example ϵ-samples ([4],[3]) which use the smallest distance of a sample point to the medial axis of the solid (i.e. the ϵ). Since a trimmed surface may be close or far from the medial axis, such criteria do not apply for surface triangulations.

In [7], The ball pivoting algorithm, (BPA), is presented. It computes a triangle mesh interpolating a given point cloud: 3 points form a triangle if a ball of radius smaller than ρ (a user specified radius) touches them without containing any other point. This triangle is a Gabriel 2-simplex in $\mathbb{R}^3$. The algorithm makes a region of triangles grow by adding a triangle to one of the boundary edges of the triangle mesh. The reconstruction algorithm needs a very uniform sample.

In [19] the intrinsic Delaunay triangulation of a Riemannian manifold is shown to be well defined in terms of geodesics. A smooth surface embedded in $\mathbb{R}^3$ can define a Riemannian manifold. The Riemannian manifolds have the property that if all the calculations and definitions are done in a small subset of the manifold, (as they can be done with a good sampling condition), the Delaunay triangulation and the Voronoi diagram are defined exactly as with the euclidean metric and are dual. Although defining triangulations with geodesics is theoretically sound, it has a prohibitively high complexity because it implies the solution of simultaneous algebraic systems.

In [2] the Gabriel complex is defined for $\mathbb{R}^n$. For a set of points in $\mathbb{R}^3$ the Gabriel complex is composed of triangles whose smallest defined circumsphere is free of points in the set. The advantage with respect to [12] is that it does not need information about the surface. The Umbrella filter algorithm described produces topologically correct triangulations. Our article takes advantage of such a definition, along with a curvature - sensitive point sample.

[5] gives lower bounds for densities of well distributed points in surfaces, based on Delaunay triangulations. [11] presents an algorithm to sample and triangulate a surface, but it uses computer expensive and not common operations. In [8] the concept of loose ϵ-sample is developed but the operations which implement it are computationally expensive.

[9] presents the Lipschitz-samples, analogous to ϵ-samples, but applied to piecewise smooth (Lipschitz) surfaces. Such a distance permits to sample a Lipschitz surface and to define a mesh on it. However, [9] does not present actual examples of the performance of the algorithm (as we do here). We do also address the sampling of edges which bound two incoming smooth surfaces by using the most larger of the two involved curvatures.

In [13], the greedy Delaunay - based surface reconstruction algorithm from a point sample is presented. The algorithm uses the fact that the Gabriel graph is a subset of the Delaunay triangulation (DT). From a starting triangle, it grows matching each of the edges in the boundary with a triangle in the DT that has the minimum radius.

As disadvantages, we may note that the algorithm: (i) requires the usual distance for Delaunay triangulations, (ii) needs a very uniform sampling in the loops and (ii) does not provide guarantee in the reconstruction.

[1] is focused in the notion of envelope that is the covering of a 3-manifold created with spheres of λ size and centered in the points of the surface. From the envelope a surface with boundaries can be reconstructed, but this approach does not conserve the original points sampled in the boundary, and parameters are needed. In practice the envelope approach does not seem to produce topologically correct results. We dispose of information about the surface and boundaries and use another approach to the problem.

In [14] an advancing front method to triangulate parametric surfaces is presented. The method triangulates a B-Rep by discretizing edges and surfaces. The number of triangles generated can be adapted to any density function in the surface. The correctness of the solution depends on the density function provided for the edges and for the surface. In [6] a parameterization-independent algorithm is proposed to triangulate a surface. In the algorithm, a circle in the normal plane of a point p in the surface S, $Tp\,(S,p)$, is chosen. A polygon of n sides, (with $n \geq 4$), and defined by vertices $\{p_1, p_2, ..., p_n\}$, is inscribed in the circle. Rays from the vertices and perpendicular to $Tp\,(S,p)$, intersect the surface and generate new vertices for the triangulation. The algorithm has the advantage that the connectivity of the triangles is present through the algorithm. In the other side, the paper handles the boundary in the parameter domain and reports a non-uniform sample near to this. The paper reports problems are in regions of high curvature. Also in [21], the algorithm described in this paper is implemented and problems are reported near the boundaries. The generalization of their algorithm to closed surfaces needs a sewing procedure that creates additional borders. In [23], an algorithm that triangulates parametric surfaces is presented. The algorithm uses an advancing front method. The loops aren't taken into account. This algorithm generates two fronts of triangles that advance one towards the other. The two fronts are in opposite sides of the parameter space. The main drawback in this algorithm is that: only a squared parameter space is considered. No holes or complex features are reported in the paper. In [22] an algorithm to triangulate b-reps is presented. In the algorithm all the triangulation occurs in parametric space and is mapped to $\mathbb{R}^3$. In [21] two sampling methods and a triangulation algorithm are proposed. In the algorithm the boundaries are isosampled, i.e not sensitive to the curvature or any other parameter. In the triangulation algorithm, a parametric information is needed, so it can fix problems, and the boundaries are not handled well in all the situations.

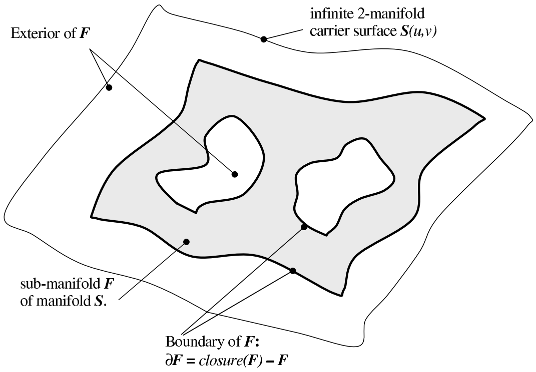

Figure 1.4: Interior, boundary and exterior of a submanifold F with respect to a manifold S.

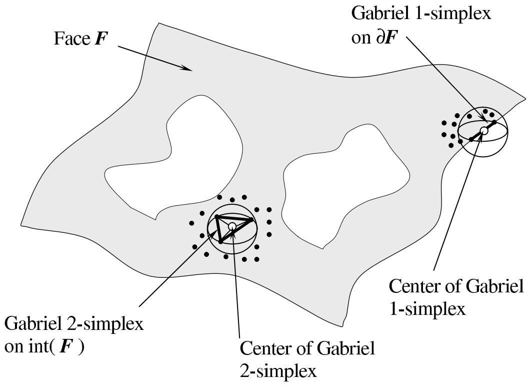

Figure 1.5: Gabriel 1- and 2-simplices on face F

1.3 Methodology

The implemented algorithm to triangulate a face F mounted onto a parametric surface S (Fig. 1.4) has the following layout, whose details will be discussed later: (1) Calculate the pre-image F^{-1} of the face F through the function S (Fig. 1.2). (2) Initialize the vertex set V_T with a curvature-sensitive sample of the loops $L_0, ..., L_n$ of the face boundary ∂F. (3) Introduce points in the sampled loops $L_0, ..., L_n$; such that, all the segments in ∂F are Gabriel 1-simplex. (4) Sprinkle the face F with vertices v_i achieving a vertex density proportional to the local curvature of F, K_{max}, inserting those vertices in set V_T. Segments in ∂F remain Gabriel 1-simplex during this stage. (5) Calculate a Gabriel connectivity T for the vertex set V_T.

1.3.1 Edge Sampling

Algorithm 1 is used to produce a curvature - sensitive sample of an Edge E. Unlike previous approaches ([22]) such a sample is not an iso-distance one. Instead, the sampling interval at point p on the underlying curve C is sensitive to the largest of the maximal curvatures of S_1 and S_2 in such a point p (line 6). Notice that the curvature *of the curve* C at p needs not to be considered in addition to the surface curvatures because it will be always less than or equal to the surface maximal curvatures $(K_{max}(S_1, p), K_{max}(S_2, p))$.

Algorithm 1 Sample of the Edge E between Faces F_1 and F_2

$S_1(u, v), S_2(u, v)$: Underlying surfaces for Faces F_1 and F_2.
$C(\lambda)$: Underlying Curve for E.
Λ_0, Λ_f: Parameters of the extremes of E in curve C.
$V_E = \{p_1, p_2, ..., p_n\}$: Output. Sequence of point sample of E.
$K_{max}(S, p))$: Maximal curvature of Surface S at point p.
N_{sides}: Number of sides of a regular polygon.

```
1:  $V_E = \{\}$
2:  $\lambda = \Lambda_0$
3:  while $\lambda \leq \Lambda_f$ do
4:      $p = C(\lambda)$
5:      $V_E = V_E \cup \{p\}$
6:      $k = max(K_{max}(S_1, p), K_{max}(S_2, p))$
7:      $r = 1/k$
8:      $\delta = polygon\_determined\_arc(r, N_{sides})$
9:      $\Delta\lambda = dist\_to\_param(\delta)$
10:     $\lambda = \lambda + \Delta\lambda$
11: end while
```

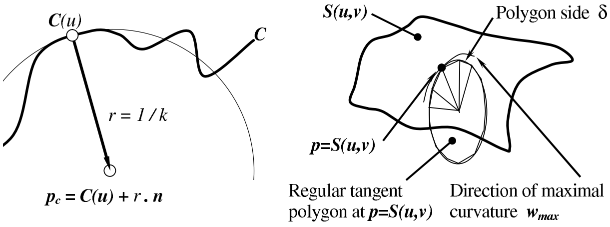

Figure 1.6: Locally planar curve and local curvature. Approximation by regular polygon of N sides.

Fig. 1.6 displays the geometrical idea behind lines 7 and 8 of the algorithm: the radius of curvature r is the inverse of the curvature k. A circle tangent to a curve with such a curvature may be approximated by a regular polygon of N_{sides} sides. The arc δ determined by such a polygon is considered as a good euclidean sampling distance for the curve C at p (line 8). Such an euclidean distance must be transformed to a local parameter distance $\delta\lambda$ at $C(\lambda)$ (line 9).

1.3.2 Loop Resampling. Ensuring that each edge of each loop is a Gabriel 1-simplex

Algorithm 2 creates new vertices in the loops sampled by algorithm 1, in such a way that each segment in the new sample is a Gabriel 1-simplex. Between lines 4 and 16, each loop V_{Li} is traversed as a circular linked list. Each segment $v_{curr}v_{next}$ is tested to be a Gabriel 1-simplex in line 7. If it is not a Gabriel 1-simplex, a new point, returned by function $point\_middle\_of\_arc$ (lines 8 and 9), is inserted to the circular linked list after v_{curr} and previous to v_{next} (lines 10 and 11). Let $C_z(\lambda)$ be a curve parameterized by arc length. Let p_x and p_y be two points in $C_z(\lambda)$. Let Λ_x and Λ_y be the parameters of p_x and p_y respectively with $\Lambda_x < \Lambda_y$. Function $point\_middle\_of\_arc\left(C_z(\lambda), p_x, p_y\right)$ performs the following procedure:

1. Finds the arc length δ between p_x and p_y in curve $C_z(\lambda)$.
2. Returns a point $p_{new} = C\left(\Lambda_x + \frac{\delta}{2}\right)$.

If any segment $v_{curr}v_{next}$ is not Gabriel 1-simplex, the variable $finished$ is set to $false$ (line 12). In line 21 the variable $finished$ is tested $true$, to ensure that this procedure is repeated until all segments are Gabriel 1-simplex.

Fig. 1.7 shows the behavior of algorithm 2. In Fig. 1.7(a), point $v_x \in V_{Li}$ is inside $B_G(v_{curr}, v_{next})$ and segment $v_{curr}v_{next}$ is not Gabriel 1-simplex. After v_{new} is inserted to V_{Li}, the new segments are (v_{curr}, v_{new}) and (v_{new}, v_{next}). As shown in Fig. 1.7(b), $B_G(v_{curr}, v_{new})$ and $B_G(v_{new}, v_{next})$ are empty of other points in $V_{\partial F}$; and segments (v_{curr}, v_{new}) and (v_{new}, v_{next}) are Gabriel 1-simplex.

Sometimes, B-rep models are not well stitched ([24]), and that creates extremely narrow faces. Every time the loop between lines 1 and 21 is executed, at least 2 segments become shorter. In line 18, function $is\_any\_segment\_too\_short\left(V_{\partial F}\right)$ evaluates this case and returns failure when an edge is too short (i.e the loop is being repeated too many times). This adds robustness to algorithm 2. Otherwise, if two lines of a b-rep are geometrically equal, but have not been merged in the model, algorithm 2 would never stop.

1.3.3 Face Sampling. Vertex Sprinkle on Face F

Algorithm 3 constructs the vertex set V_F of the triangulation sought for face F. The initialization of V_F (line 1) is done with the vertices sampled on the boundary loops of F, $\partial F = \{L_0, ..., L_n\}$, as per algorithm 1. Such vertices correctly sample ∂F. However, the interior $int(F)$ needs to be sampled. To do so, trial vertices are generated inside the pre-image F^{-1} in $U \times V$ space (line 4) and their image via S is

Algorithm 2 Insert vertices in the sampled loops until all the segments are Gabriel 1-simplex.

$V_{\partial F} = \{V_{L1}, V_{L2}, V_{Ln}\}$: is the set of vertices that sample the boundary of the face F.
$V_{Li} = \{V_{E1}, V_{E2}, ..., V_{Em}\}$: is a circular linked list that contains all the points sampled in the loop with algorithm 1 and V_{Ej} is the ordered sample of edge E_j.
$V_{\partial F} = \{V_{L1}, V_{L2}, V_{Ln}\}$. Output. The set of vertices that sample the boundary of face F.

```
repeat
  $finished = true$
  for all $V_{Li} \in V_{\partial F}$ do
    $v_{curr} = head\left(V_{Li}\right)$
    $v_{next} = next\left(V_{Li}, v_{curr}\right)$
    repeat
      if $\exists v_x \in \left(V_{Li} - \{v_{curr}, v_{next}\}\right)$,
      such that: $v_x \in B_G\left(v_{curr}, v_{next}\right)$ then
        $C_j\left(\lambda\right)$ is the curve, of an edge $E_j$, that contains $\{v_{curr}, v_{next}\}$.
        $v_{new} =$
          $point\_middle\_of\_arc\left(C_j\left(\lambda\right), v_{curr}, v_{next}\right)$.
        $next\_of\left(V_{Li}, v_{curr}\right) = v_{new}$
        $next\_of\left(V_{Li}, v_{new}\right) = v_{next}$
        $finished = false$
      end if
      $v_{curr} = v_{next}$
      $v_{next} = next\left(V_{Li}, v_{next}\right)$
    until $v_{curr} \equiv head\left(V_{Li}\right)$
  end for
  if $is\_any\_segment\_too\_short\left(V_{\partial F}\right)$ then
    return $FAILURE$
  end if
until $finished \equiv true$
```

Algorithm 3 Sprinkle triangulation vertices on Face F

F: Input. Face to triangulate.
F^{-1}: pre-image of Face F in space $U \times V$
$S(u,v)$: Underlying surface for Face F.
$\partial F = \{L_0, ..., L_n\}$: Loops Bounding the Face F.
N_f: Number of tolerated failures.
V_F: Output. Vertex set sampled on Face F.

```
$V_F$ = sampling of boundary $\partial F$
$fails = 0$
while $fails \leq N_f$ do
    generate parameter pair $(u,v) \in F^{-1}$
    $k = K_{max}(S(u,v))$
    $r = 1/k$
    $p = S(u,v)$
    $R = polygon\_side(r, N_{sides})$
    if $\nexists q \in V_F$ such that $q \in B(p,R)$ then
        if $\exists v_i v_j$, a segment of the boundary, such that: $p \in B_G(v_i, v_j)$ then
            $fail = fail + 1$
        else
            $V_F = V_F \cup \{p\}$
            $fail = 0$
        end if
    else
        $fail = fail + 1$
    end if
end while
```

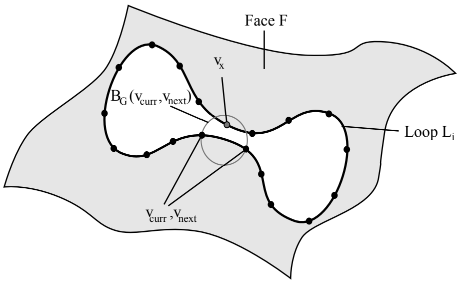

(a) First a sampled vertex v_x is inside of $B_G\ (v_{curr}, v_{next})$. Segment (v_{curr}, v_{next}) is not Gabriel 1-simplex.

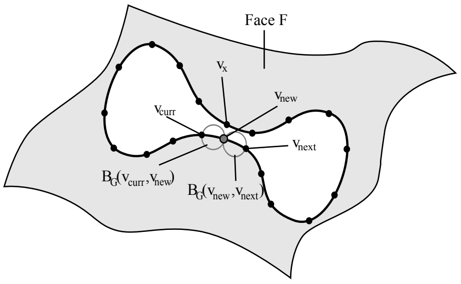

(b) When algorithm 2 inserts v_{new}, segment $v_{curr}v_{next}$ is replaced by segments $v_{curr}v_{new}$ and $v_{new}v_{next}$. No point sampled is inside balls $B_G\ (v_{curr}, v_{new})$ and $B_G\ (v_{new}, v_{next})$. Segments $v_{curr}v_{new}$ and $v_{new}v_{next}$ are Gabriel 1-simplex.

Figure 1.7: The two basic steps of algorithm 2.

calculated (line 7). Such a trial vertex p is rejected if (a) it is too close to other vertices already accepted in V_F (line 11) or (b) if it is contained in the smallest ball defined by a pair of vertices consecutive on a loop L_j. The closeness criteria is dictated by the maximal curvature $K_{max}(S(u,v))$ at $p = S(u,v)$ (line 5). In case (a) each already accepted vertex in V_f is tested for inclusion inside a ball $B(p,R)$ centered at p with radius $R = polygon\_side(r, N_s ides)$ (line 9). In case (b) each segment v_iv_j in the sample of the border is tested as a Gabriel segment (1-simplex) with respect to the candidate p. If every segment of the border is Gabriel with respect to p, we assume that p is not too close to the border (line 10). A segment is said to be *sampled in the boundary*, if its two end vertices are consecutive in a loop $L_j \in \partial F$. If tests (a) and (b) are passed, p is accepted in V_F (line 13). Fig. 1.6 depicts that the value for R is computed as the cord of the N_{sides}-regular polygon inscribed in the circle with radius $1/k$. Function $polygon\_side(r, N_s ides)$ equals to $2r\sin(\pi/N_s ides)$. Fig. 1.5 displays the two tests mentioned in items (a) and (b) above.

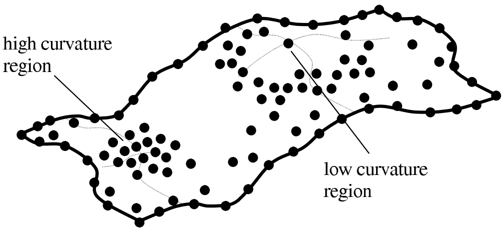

Figure 1.8: Goal Point Population on face F

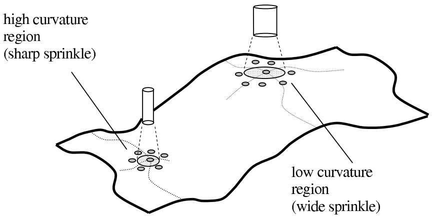

Figure 1.9: Curvature-sensitive Sprinkle Airbrush F

1.3.4 Face Triangulation. Gabriel Connectivity on Vertex Set V_T.

Algorithm 4 builds the connectivity inside the vertex set V_F. The algorithm seeks to complete edges (v_0, v_1) already known to belong to the triangulation T (line 6) with an additional vertex v_{new} to build a Gabriel Triangle (v_0, v_1, v_{new}) (line 9).

Any internal Gabriel triangle is the first formed triangle (lines 1,4). It is also a seed to initialize the $Queue$ of edges potentially able to span Gabriel triangles.

If the edge extracted from the $Queue$ is part of the boundary, it is not expanded any more (line 7). All the edges which are part of the boundary will be found because they are Gabriel 1-simplex and make part of a Gabriel 2-simplex. If a Gabriel triangle (v_0, v_1, v_{new}) can be built, it is added to the triangulation T (line 10). If a Gabriel triangle can be built using only an existing edge (v_0, v_1) and a new vertex v_{new}, the general situation is that the new edges (v_0, v_{new}) and (v_{new}, v_1) should be queued to be eventually expanded (line 20). However, this is not always the case, since such a triangle may use 1 or 2 *additional* edges already in the queue. In the first case, the triangle is filling a corner (lines 13-18). In the second case, the triangle is filling a triangular hole (lines 11,12). In such special cases additional edges (1 or 2 besides the expanded one) should be taken away from the queue.

Algorithm 4 Triangle Connectivity in the set V_F

V_F: Input. Vertex set sampled on Face F.
$Queue$: List of triangle edges to expand.
$\partial F = \{L_0, ..., L_n\}$: Loops Bounding the Face F.
T: Output. Triangulation.

```
$seed = triangle\_in\_interior(F)$
$\{(v_0, v_1), (v_1, v_2), (v_2, v_0)\} = edges\_of\_triang(seed)$
$Queue = \{(v_0, v_1), (v_1, v_2), (v_2, v_0)\}$
$T = \{\ seed\}$
while ($Queue \neq \Phi$) do
    $edge\_to\_expand = extract(Queue)$
    if $edge\_to\_expand$ is not part of the sample of the boundary then
        $(v_0, v_1) = vertices(edge\_to\_expand)$
        $v_{new} = vert\_for\_Gabriel\_2\_Simplex(V_F, v_0, v_1)$
        $T = T \cup \{(v_0, v_1, v_{new})\}$
        if $((v_0, v_{new}) \in Queue) \wedge ((v_{new}, v_1) \in Queue)$ then
            $Queue = Queue - \{(v_0, v_{new}), (v_{new}, v_1)\}$
        else if $((v_0, v_{new}) \in Queue)$ then
            $Queue = Queue - \{(v_0, v_{new})\}$
            $Queue = Queue \cup \{(v_1, v_{new})\}$
        else if $((v_{new}, v_1) \in Queue)$ then
            $Queue = Queue - \{(v_{new}, v_1)\}$
            $Queue = Queue \cup \{(v_{new}, v_0)\}$
        else
            $Queue = Queue \cup \{(v_1, v_{new}), (v_{new}, v_0)\}$
        end if
    end if
end while
```

1.4 Complexities of the algorithms

Time and space complexities of all the algorithms were found. They are all output sensitive; that is, their complexities depends on the size of the output given by them. The first 3 algorithms depend on the number of nodes generated by them. The last algorithm depends on the number of nodes in the input and in the number of triangles generated.

1.4.1 Edge Sampling

The time and space complexities of algorithm 1, have been found in the following manner.

1. Time complexity. The operations with the curve and the operations to find the curvatures are dependent upon the parameterization and not in the number of points generated. Because of this, the time complexities of all the operations within the loop, (lines 3 to 11), can be assumed as $O(1)$. The loop is repeated N_{Ej} times. N_{Ej} is the number of points generated to sample the edge E_j. The time complexity of algorithm 1 is $O(N_{Ej})$.
2. Space complexity. As the algorithm only stores the points generated, the space complexity is $O(N_{Ej})$.

1.4.2 Loop Resampling

The time and space complexities of algorithm 2, have been found in the following manner:

1. Time complexity. Let $N_{\partial F}$ be the number of vertices in $V_{\partial F}$, at the end of algorithm 2. For algorithm 2 the following facts hold:
    (a) $N_{\partial F}$ changes. In the worst case it grows as an arithmetic progression with difference 1. That is why in this paper the calculations are simplified by considering, at any step, $N_{\partial F}$ as the number of vertices in $V_{\partial F}$.
    (b) The number of segments in $V_{\partial F}$ is the same as the number of points.
    (c) Each time a segment $v_{curr}v_{next}$ is tested to be Gabriel 1-simplex, (line 7), algorithm 2 tests all the points in $V_{\partial F}$. This takes time $O(N_{\partial F})$.
    (d) The number of segments tested will be $O(N_{\partial F})$, no matter the number of points added to the sample in the previous step.
    (e) The worst case scenario occurs when only one point is added at the time. This is because of fact (d). In that case, the loop from lines 1 to 21 is repeated $N_{\partial F}$ times.

    (f) The worst case scenario occurs when only 3 vertices have been generated by algorithm 1. This is the worst case because it means that all but 3 of the points in $V_{\partial F}$ are generated by algorithm 2. The number of times that the loop between lines 1 to 21 is repeated is $O\left(N_{\partial F}\right)$.

   Combining facts (c), (d) and (e) the worst case time complexity of the algorithm 2 is $O\left(N_{\partial F}^{3}\right)$.

2. Space complexity. Only $V_{\partial F}$ is stored by the algorithm. The space complexity of algorithm 2 is $O\left(N_{\partial F}\right)$.

1.4.3 Face Sampling

The time and space complexities of algorithm 3, have been found in the following manner:

1. Time complexity. The algorithm terminates if variable $fails > N_f$; so for each new point, the algorithm tries at most N_f times. The number of times that the loop between lines 3 and 19 is $O\left(N_f \times N\right)$, being N_F the number of points generated in the interior of the face. In the loop, for a new generated point p two tests are performed:

    (a) In line 9, every $q \in V_F$ is tested for inclusion in $B\left(p, R\right)$. R is as described in line 8. This operation can be performed in $O\left(N_F + N_{\partial F}\right)$.

    (b) In line 10, p is tested for inclusion in every $B_G\left(v_i, v_j\right)$, where $v_i v_j$ are two consecutive points in the sample of the boundary of F. This operation can be performed in $O\left(N_{\partial F}\right)$.

   The worst complexity is that of test (a).

   Combining test (a) with the number of times the loop between lines 3 and 9 is repeated, we have that the complexity of the algorithm is: $O\left(N_f \times N_F\left(N_F + N_{\partial F}\right)\right)$.

2. Space complexity. The algorithm only stores the points that are accepted. The space complexity of the sampling algorithm is $O\left(N_F\right)$.

1.4.4 Face Triangulation

The time and space complexities of the algorithm 4, have been found in the following manner.

1. Time complexity. For algorithm 4, the following facts hold:

   (a) Each time that the loop (lines 5 to 23) is repeated, this algorithm checks a different edge that belongs to the triangulation. The number of edges that belong to the triangulation is a linear function of the number of triangles (i.e each new triangle adds a maximum of 3 edges). The number of triangles generated will be denoted as: N_T.

   (b) The operation *vert_for_Gabriel_2_Simplex* (line 9), is the one that has the highest complexity within the loop (lines 5 to 23). The rest of the operations have $O(1)$ complexity.

   (c) For the *vert_for_Gabriel_2_Simplex* (line 9) operation, first a candidate vertex (r) is chosen. This vertex can complete a Gabriel simplex given the edge v_0v_1. All the points in V_F, except for v_0 ,v_1 and r are tested for inclusion in $B_G(v_0, v_1, r)$. Using a naive approach, the time complexity of this operation would be $O\left(N^2\right)$, where N is the number of vertices in V_F.

   Combining facts (a), (b) and (c), the complexity of algorithm 4 is $O\left(N_T \times N^2\right)$.

2. Space complexity. The algorithm stores a set of edges in $Queue$. As a topological constrain, $Queue$ can only contain the same edge twice. The number of edges stored is, in the worst case, a linear function of the number of triangles stored. The space complexity is $O(N_T)$.

1.5 Results

Several Boundary Representations B-Reps were used to test the implemented algorithm, proposed in this article. Such B-reps have genera 3 or superior, and present faces F whose underlying surfaces S are parametric ones of the NURBS or Spline types. An $N_f = 1000$ maximal number of failed trials was used to stop the sprinkle of vertices on F (generation of the set V_F). The number of sides for the approximating polygon was $N_{sides} = 30$. Figs. 1.10, 1.11 and 1.13 show complex B-Reps. Other examples of B-reps triangulated include a model of a pre-columbian fish in Fig. 1.14, a support of an axle in Fig. 1.15, and a stub axle in Fig. 1.16.

The attention of the reader is called to the fact that the connectivity construction is a process completely independent of the vertex generation process. Since the vertex generation algorithm (Sprinkle) is the most critical one, the execution time was recorded for such an aspect.

For the models *Pump* and *Hands*, Figs. 1.12(a) and 1.12(b) show execution times, corresponding to the vertex generation process. Fig. 1.12(c) shows the comparison of vertex generation times for such runs.

Figure 1.10: Pump carter [17]. Colormap according to quality of triangles.

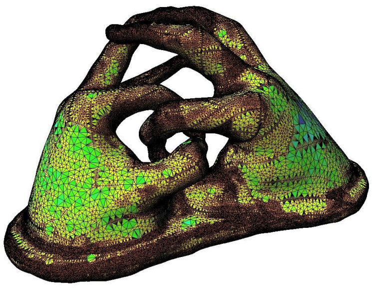

Figure 1.11: 2 hands with 3 genus, scanned and reconstructed using RainDrop Geomagic. Colormap according to the size of the triangles

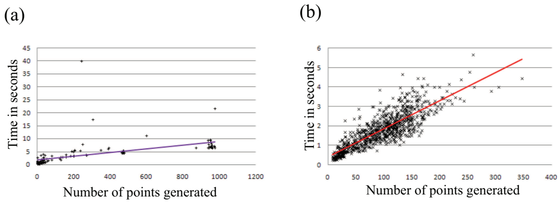

(a) Sample time per face for the pump.

(b) Sample time per face for the two hands.

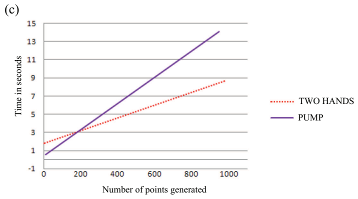

(c) Comparison between the hands (NURBS) and the Pump Carter. Hands time in solid line, Pump time in dotted line

Figure 1.12: Times spent sampling the faces and their comparison.

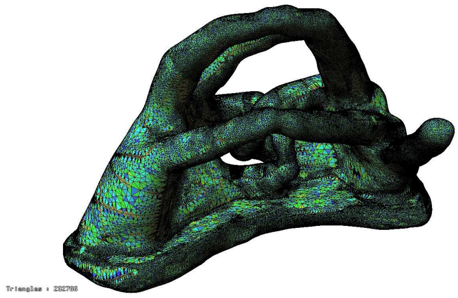

Figure 1.13: Other view of the 2 hands with 3 genus. Colormap according to the quality of the triangles.

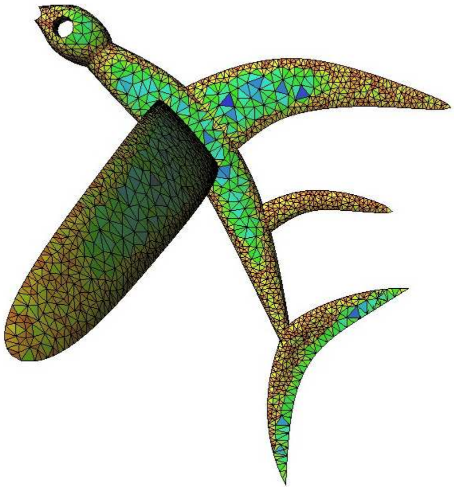

Figure 1.14: Artificial replica of a pre-columbian gold fish [15]. Colormap according to size of the triangles

1.6 Conclusions and future work

The proposed algorithm for generating triangulation vertex sets and for calculating the connectivity among them proved to function correctly, even for very extreme geometries and topologies. Several aspects of the algorithm must be addressed: the continuity of triangle sizes at the Face Edges, the possibility of undertaking re-meshing of already existing triangulations and its related endeavor, namely the level of detail, necessary for Finite Element Analysis applications. Additional research is needed in algorithms that (i) take advantage of the concepts presented in the heuristic algorithm proposed here, but (ii) can be proved correct.

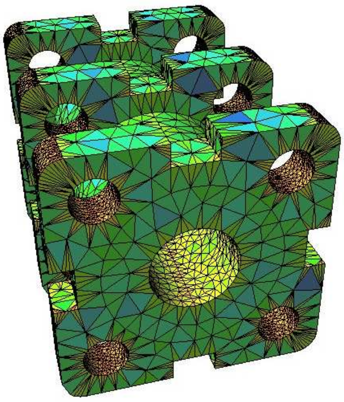

Figure 1.15: Support of an axle. Colormap according to size of the triangles

Figure 1.16: Stub axle [18]. Colormap according to the quality of the triangles

Bibliography

[1] K. Abe, J. Bisceglio, T. J. Peters, A. C. Russell, and T. Sakkalis. Computational topology for reconstruction of surfaces with boundary: Integrating experiments and theory. In *SMI ’05: Proceedings of the International Conference on Shape Modeling and Applications 2005*, pages 290–299, Washington, DC, USA, 2005. IEEE Computer Society.

[2] Udo Adamy, Joachim Giesen, and Matthias John. New techniques for topologically correct surface reconstruction. In *VIS ’00: Proceedings of the conference on Visualization ’00*, pages 373–380, Los Alamitos, CA, USA, 2000. IEEE Computer Society Press.

[3] N. Amenta, M. Bern, and D. Eppstein. The crust and the beta-skeleton: Combinatorial curve reconstruction. *Graphical models and image processing: GMIP*, 60(2):125–, 1998.

[4] Nina Amenta and Marshall Bern. Surface reconstruction by voronoi filtering. In *SCG ’98: Proceedings of the fourteenth annual symposium on Computational geometry*, pages 39–48, New York, NY, USA, 1998. ACM.

[5] Dominique Attali, Jean-Daniel Boissonnat, and André Lieutier. Complexity of the delaunay triangulation of points on surfaces the smooth case. In *SCG ’03: Proceedings of the nineteenth annual symposium on Computational geometry*, pages 201–210, New York, NY, USA, 2003. ACM.

[6] Marco Attene, Bianca Falcidieno, Michela Spagnuolo, and Geoff Wyvill. A mapping-independent primitive for the triangulation of parametric surfaces. *Graphical Models*, 65(5):260 – 273, 2003. Special Issue on SMI 2002.

[7] Fausto Bernardini, Joshua Mittleman, Holly Rushmeier, Claudio Silva, and Gabriel Taubin. The ball-pivoting algorithm for surface reconstruction. *IEEE TRANSACTIONS ON VISUALIZATION AND COMPUTER GRAPHICS*, 5(4):349–359, 1999.

[8] J-D Boissonnat and S. Oudot. An effective condition for sampling surfaces with guarantees. In *SM '04: Proceedings of the ninth ACM symposium on Solid modeling and applications*, pages 101–112, Aire-la-Ville, Switzerland, Switzerland, 2004. Eurographics Association.

[9] Jean-Daniel Boissonnat and Steve Oudot. Provably good sampling and meshing of lipschitz surfaces. In *SCG '06: Proceedings of the twenty-second annual symposium on Computational geometry*, pages 337–346, New York, NY, USA, 2006. ACM.

[10] Manfredo Do Carmo. *Differential geometry of curves and surfaces*, pages 1–168. Prentice Hall, 1976. ISBN: 0-13-212589-7.

[11] Siu-Wing Cheng, Tamal K. Dey, Edgar A. Ramos, and Tathagata Ray. Sampling and meshing a surface with guaranteed topology and geometry. In *SCG '04: Proceedings of the twentieth annual symposium on Computational geometry*, pages 280–289, New York, NY, USA, 2004. ACM.

[12] L. Paul Chew. Guaranteed-quality mesh generation for curved surfaces. In *SCG '93: Proceedings of the ninth annual symposium on Computational geometry*, pages 274–280, New York, NY, USA, 1993. ACM.

[13] David Cohen-Steiner and Frank Da. A greedy delaunay based surface reconstruction algorithm. Research report, INSTITUT NATIONAL DE RECHERCHE EN INFORMATIQUE ET EN AUTOMATIQUE, 2002.

[14] JC Cuillière. An adaptive method for the automatic triangulation of 3d parametric surfaces. *Computer-Aided Design*, 30(2):139 – 149, 1998.

[15] Museo del Oro Bogotá DC. Pre-columbian fish. http://www.banrep.org/museo/eng/home4.htm.

[16] Herbert Edelsbrunner and Nimish R. Shah. Triangulating topological spaces. In *SCG '94: Proceedings of the tenth annual symposium on Computational geometry*, pages 285–292, New York, NY, USA, 1994. ACM.

[17] Rosalinda Ferrandes. Pump carter. http://shapes.aimatshape.net/viewgroup.php?id=919.

[18] Rosalinda Ferrandes. Stub axle. http://shapes.aimatshape.net/viewgroup.php?id=917.

[19] Greg Leibon and David Letscher. Delaunay triangulations and voronoi diagrams for riemannian manifolds. In *SCG '00: Proceedings of the sixteenth annual symposium on Computational geometry*, pages 341–349, New York, NY, USA, 2000. ACM.

[20] Ángel Montesdeoca. Apuntes de geometría diferencial de curvas y superficies. Santa Cruz de Tenerife, 1996. ISBN: 84-8309-026-0.

[21] Oscar Ruiz, John Congote, Carlos Cadavid, and Juan G. Lalinde. A curvature-sensitive parameterization-independent triangulation algorithm. In *5th Annual International Symposium on Voronoi Diagrams in Science and Engineering. 4th International Kyiv Conference on Analytic Number Theory and Spatial Tessellations. (Kokichi Sugihara and Deok-Soo Kim, eds.)*. Drahomanov National Pedagogical University, 2008.

[22] Oscar E. Ruiz and Sebastian Peña. Aspect ratio- and size-controlled patterned triangulations of parametric surfaces. In *Ninth IASTED Intl. Conf. Computer Graphics and Imaging*, February 13-15 2007.

[23] Baohai Wu and Shangjin Wang. Automatic triangulation over three-dimensional parametric surfaces based on advancing front method. *Finite Elements in Analysis and Design*, 41(9-10):892 – 910, 2005.

[24] Hong-Tzong Yau, Chuan-Chu Kuo, and Chih-Hsiung Yeh. Extension of surface reconstruction algorithm to the global stitching and repairing of stl models. *Computer-Aided Design*, 35(5):477 – 486, 2003.

Chapter 2

Simulation of the handling in green of ceramic tiles with deep back relief

Context

The CAD CAM CAE Laboratory at EAFIT University has kept throughout the years cooperation agreements with research universities and institutions in Europe including: *Max-Planck-Institut fur Informatik* at *Universitt des Saarlandes*, Saarbrcken, Germany, Fraunhofer Inst. *Graphische Datenverarbeitung*, Darmstadt, Germany, the University of Vigo, Vigo, Spain and the *Universidad Politécnica de Valencia*, Valencia, Spain. As a part of such agreements, students hold visiting research assistant positions at the hosting institution for periods ranging from 6 to 12 months.

Ricardo Serrano has been invited by Prof. Guillermo Peris Fajarnes, director of the *Centro de Investigación en Tecnologías Gráficas* at the *Universidad Politécnica de Valencia*, Valencia, Spain to join his group as visiting research assistant. During his internship, (October 2008-April 2009), Ricardo participated in the development of a software for the evaluation of the ceramic tiles manufacturing process.

The software developed used knowledge in the fields of Computational Geometry, Geometric Modeling, Computer Assisted Design, Computer Assisted Engineering, Finite Element Analysis, Mechanics of Materials and Software Development in the TCL/TK language and in ANSYS® Parametric Design Language (APDL). This research has application in the fields of Computer Aided Engineering and Ceramics Manufacturing. The research is very important for the Ceramics Manufacturing field because it helps to evaluate the possible designs so they not only comply with the regulations and quality standards but also withstand the different handling processes.

The work is yet unpublished.

As coauthors of the publications we give the permissions for this material to appear in this document. We are ready to provide any additional information on the subject, as needed.

Prof. Dr. Ing. Guillermo Peris Fajarnes
gperis@degi.upv.es
Director *Centro de Investigación en Tecnologías Gráficas*
Universidad Politécnica de Valencia
Valencia, Spain

Dra. Ing. Beatriz Defez García
bdefez@degi.upv.es
Assistant Professor *Centro de Investigación en Tecnologías Gráficas*
Universidad Politécnica de Valencia
Valencia, Spain

Prof. Dr. Eng. Oscar E. Ruiz
oruiz@eafit.edu.co
Coordinator CAD CAM CAE Laboratory
EAFIT University
Medellín, Colombia

Software Developed

When modeling a problem by means of the FEM, the engineer uses some general steps:

1. To model the geometry.
2. To specify boundary and initial conditions.
3. To specify the material property.
4. To mesh the geometry.

The UML (Unified Modeling Language) Activity Diagram, of the modeling a problem by means of the FEM, can be seen in figure 2.1. All the steps have to be done carefully by the user.

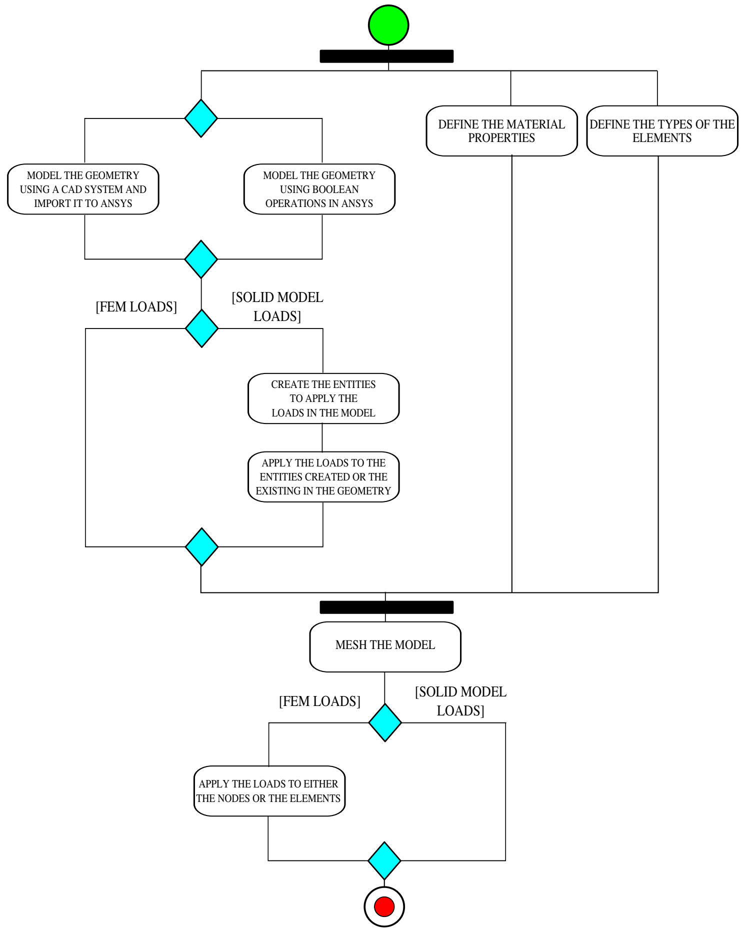

Figure 2.1: UML Activity Diagram to create an FEM model in ANSYS®.

In this project a software that automates the, sometimes arduous, process of modeling the ceramic tiles manufacturing process by means of the FEM is presented.

ANSYS® provides a command interface to the user called APDL®. Of these, the preprocessor commands are the used to model the problem and obtain the solution. Everything that can be done in the GUI can be translated to a set of APDL® commands. Since ANSYS® 5.5, TCL/TK, a scripting language designed for embedded systems, is included in the application. It was used by ANSYS® developers to create a more pleasant GUI for the user. TCL/TK can send commands written with APDL® syntax to ANSYS® which interprets and executes them. An application that allows the user to create a working FEM model in ANSYS®, using only high level parameters, was created using TCL.

The application allows the easy and fast variation of parameters in the geometry of the ceramic tile and production stages. The UML Activity Diagram to create the model with the application can be seen in figure 2.2. The user only performs a few high level steps.

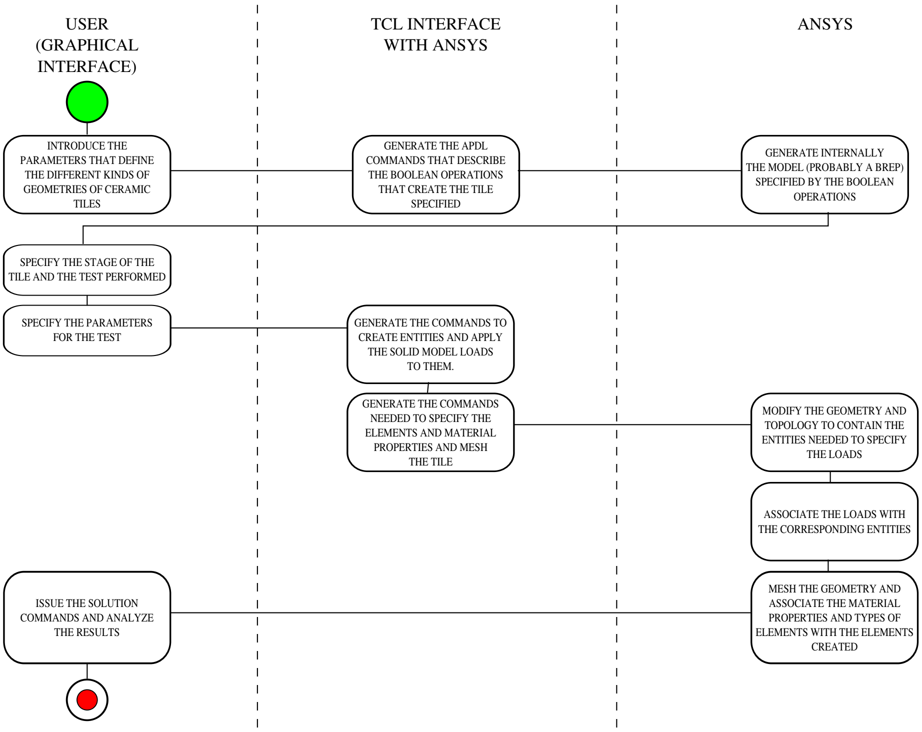

Figure 2.2: UML Activity Diagram for the software developed using TCL/TK.

Abstract

To keep its competitiveness, the Spanish ceramic industry, one of the biggest of the world, needs to reduce costs and assure quality in its products. One way to do this is to design and produce tiles with less raw material in their support. This could be done with help of the deep back relief. The design of the tiles not only needs to comply with the regulations and quality standards. It also needs to withstand the different handling processes. One of the most important stages in the development of ceramic tiles is the pressure forming and subsequent handling in green. After the tile is pressure formed, it's said to be in green state and it's in its weakest form. Computational simulations based on the finite element method, (FEM), could offer important information and save costs and development time when evaluating if the tiles can undergo the handling in green process. This paper presents the steps taken to evaluate the appropriateness of a back relief for the green handling. (i) It shows an introduction of the theories needed to apply the finite element method to some models of ceramic tiles in green state. (ii) It proposes a method to evaluate the appropriateness of a back relief. With this method, a tile with back relief is compared with tiles lightened by reducing their thickness. (iii) It makes a parametric study of the squares back relief, which was the best behaved when comparing it to the thin tiles. (iv) Generalizes the method proposed and formulates it in terms of simple calculations. The main conclusion of the paper is that the design of the back relief could have an impact the strength of the tiles during the handling in green process. It concludes, also, that a good design of back relief can compare well with a thinner tile with the same raw material.

Glossary

E:	Young's or elastic modulus.
v:	Poisson's ratio
ρ:	Bulk density of the tile
g:	The gravitation of the system. The sign convention of the gravitational acceleration denotes as positive the direction of the reaction force.
α	The angular acceleration.

2.1 Introduction

To keep its competitiveness, the Spanish ceramic industry, (the second most important of the world), needs to reduce costs and assure the quality of its products. As shown in [7] and [8], one of the possibilities that could help to reduce costs is the back relief of the ceramic tile. Back reliefs have always existed. They were present in the past to help to the ventilation during the piling phase before baking. They later fell in disuse, because of the introduction of continuous kilns and single-baking. Recently, it has been seen as a very promising approach to reduce the costs of raw material, manufacturing and handling. A non-constant thickness in the back relief of the tile could also help to increase the adherence of the tile to the concrete. Of great importance also, is the production of specifically designed tiles that allow wires or other kind of structures to be perfectly camouflaged in the decoration.

One of the stages of the ceramic tile manufacturing process is the pressure forming and the handling in green state. After the pressure forming, the tile is in its weakest state and can be easily broken. It has been shown that this stage accounts loses of around 200 million € in Europe alone ([2]). The mechanical and thermal properties of ceramic tiles are dependent on the design of the back relief ([6, 7, 8]). In green state the tile is weaker and those differences can be more important. For that reason, the strength of any proposed design need to be evaluated not only in its final properties. It also needs to be evaluated within the manufacturing stages. The traditional form of doing this is making the tiles to undergo the different processes, but producing and evaluating the designs in real life can be really expensive.

The Finite Element Method is a numerical method that seeks an approximated solution of the distribution of field variables in a problem domain ([14]). It is often used when a solution is difficult to obtain analytically. The complex geometries found in several designs of the ceramic tiles' deep back relief, make this method the most useful.

In this paper are presented:

1. A description of: (i) the problem, (ii) the theories and steps needed to model

the problem by means of the FEM and (iii) the actual considerations taken when modeling the problem by means of the FEM.

2. A method to evaluate the appropriateness of a tile with back relief, compared with a tile lightened by making it less thick. The results and analysis of these comparisons are carried out for some standard back reliefs of tiles.

3. The results and analysis of the behavior of parametric variations for some a standard kind of back relief.

4. Conclusions and future work.

2.2 Modeling the problem by means of the FEM

2.2.1 Modeling the geometry

A ceramic tile with deep back relief has the following geometric characteristics. (i) It's a box with 1 dimension significantly smaller than the other 2, which are usually equal. (ii) The thickness is non-constant and produces regular shapes. In the paper, the reference tile has dimensions $0.33\text{m} \times 0.33\text{m} \times 0.008\text{m}$. The tile can be observed in Fig. 2.3.

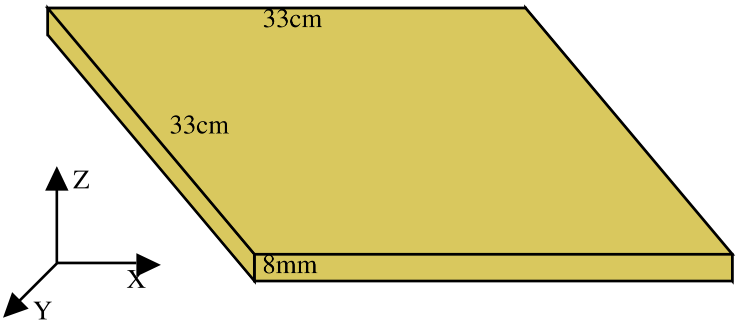

Figure 2.3: Reference tile with its dimensions.

The kinds of back reliefs modeled were 3:

1. The squares back relief is shown in Fig. 2.4. The set of squares tile the back of the support, except on the separation between them. They are extruded to form the prisms subtracted from the tile.

2. The hexagons back relief is shown in Fig. 2.5. The set of hexagons tile the back of the support, except on the separation between them. They are extruded to form the prisms subtracted from the tile.

3. The diamonds back relief is shown in Fig. 2.6. The set of squares, are rotated 45° in relation to the axes. They are extruded to form prisms and are added to the back of the tile. In this back relief a border is present.

These are some of the shapes that are found the most in the industry ([6]).

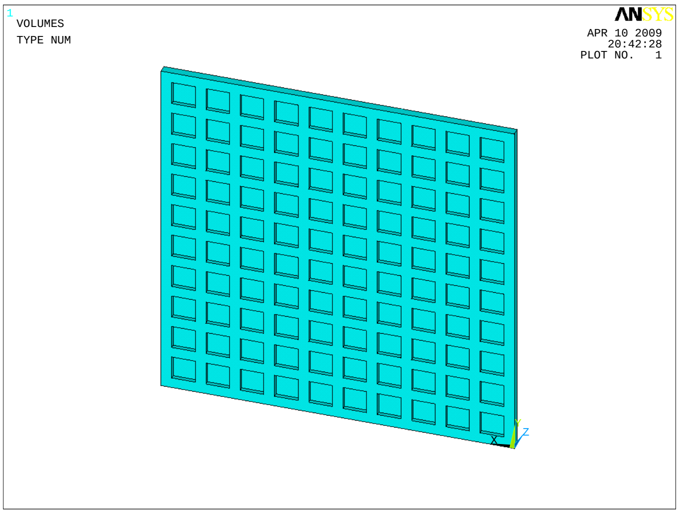

Figure 2.4: Back relief of squared prisms subtracted from the back.

The parameters used to define each back relief were: (i) the tile dimensions, (ii) the separation of the first polygon from the border, the separation of each polygon from each other, the number of polygons per row and the depth of the prisms.

2.2.2 Applying the boundary, initial and loading conditions

In ANSYS®, two kinds of loads can be applied: (i) Solid model loads and (ii) FEM loads. The solid model loads are applied to the entities. The entities can be: (i) volumes, (ii) areas, (iii) lines and (iv) keypoints. When the mesh is modified the solid model loads remain intact. That does not occur for FEM loads that are applied either to: (i) the nodes or (ii) the elements. Solid model loads have also an advantage: they can describe the geometry of the loads more correctly.

For this project solid model loads were used. The main reason was that the places, where forces needed to be applied or displacements needed to be prescribed, did not exist as separate entities and any selection of nodes did not correctly describe this places. Boolean operations of subtraction and overlapping were used to create the exact areas where the loads were to be applied independently of the model of back relief represented ([13]).

The boundary conditions, to be applied to each model of ceramic tile, were 2:

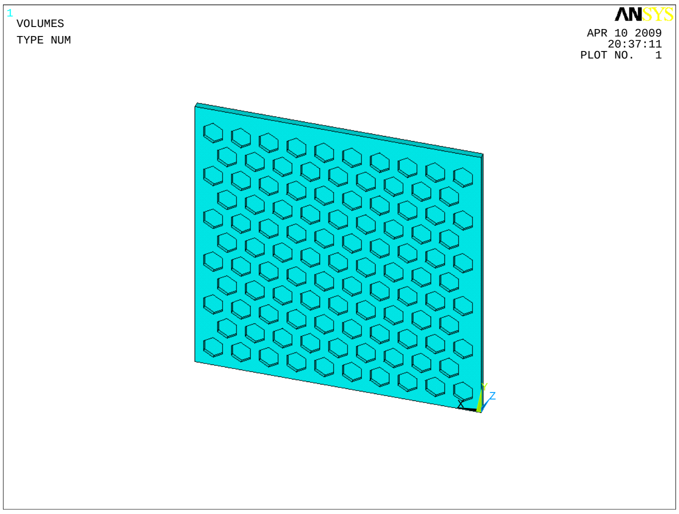

Figure 2.5: Back relief of hexagonal prisms subtracted from the back.

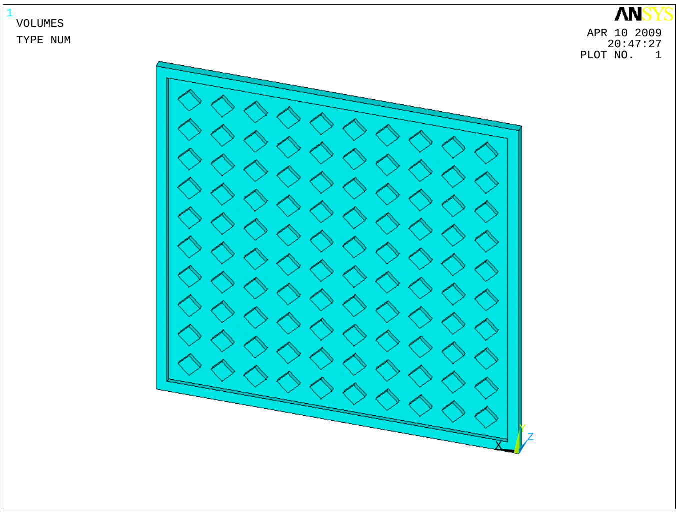

Figure 2.6: Back relief of diamond prisms added to the back.

1. The tile supported in a band and loaded by its own weight. An artistic drawing of the test can be seen in Fig. 2.7(a). The parameters of this test are:
    (a) The separation of each band from the border of the tile: 0.075m.
    (b) The width of each of the bands: 0.02m
    (c) The gravity (g): 9.81m/s^2
2. The tile in a rotational machine, and loaded by its own weight and the effect of the rotational acceleration. An artistic drawing of the test can be seen in Fig. 2.7(b). The parameters of the test are:
    (a) The separation from the center of the machine to the border of the tile: 1m.
    (b) The separation from the border closest to the center, to the first cylinder: 0.075m.
    (c) The separation between the cylinders: 0.1m.
    (d) The angular acceleration (α): 1 rad/s^2.
    (e) The gravity (g): 9.81m/s^2.

They will be called test T1 and T2 in the rest of the paper.

2.2.3 Specifying the material property

Ceramic materials are anisotropic; that is, tensile stresses can produce different elastic deformations in different directions. Because most of the materials are poly crystalline with random orientations of their grains, the variation of the Young modulus, (E), produces a uniform pattern of stresses. Because of this, the material can be threated as isotropic and the mean elastic modulus is appropriate ([15], [10]). This fact is very useful for FEM simulations of structural problems; because to define the material, only the mean Young's modulus and mean Poisson's ratio, (v), need to be provided.

Young's modulus and Poisson's ratio has been established for a very reduced number of green ceramic materials. One of the difficulties that arise with these materials, is that they are compact and brittle powders, (they don't have or they almost don't have plastic deformation); because of this, the traditional tensile specimen does not work to evaluate their behavior. As seen in [17], the main challenge consists in avoiding the premature failure related with unaligned attachments or the contact effects of the attachments. In this paper a description of the challenges and solutions to measure the mechanical properties of as pressed compacts is presented. The Weibull statistics and their application to these compacts are also explained in the paper. In [2] several techniques to analyze compact powders, (formed by pressure and in green state), are analyzed. It is shown that, unlike the three and four point flexural tests, the strength of

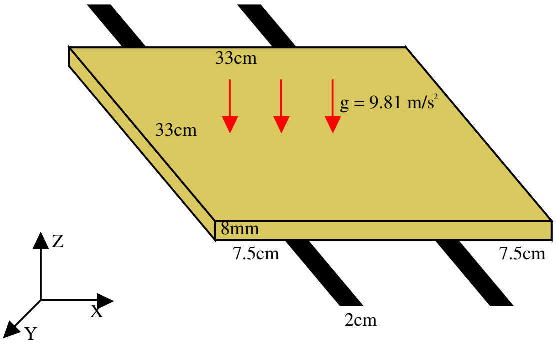

(a) Test T1. Tile supported in a band

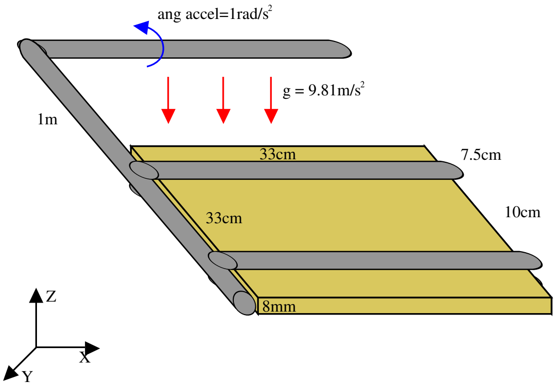

(b) Test T2. Tile in the rotational machine.

Figure 2.7: Different processes that the tiles undergo during their handling in green.

the compacts with binder in the diametral compression test is not explained entirely by Weibull statistics.

In [3], the relationship between the porosity of green porcelain tiles and the porosity of sintered porcelain tiles is shown to be very strong. The porosity is also shown to be correlated with the strength of the finished bodies.

Many green ceramics contain water and organic binders, which can make them viscoelastic. This is shown in [18]. Other authors have characterized green ceramics with binders. In the paper [12] a study of the mechanical properties in green state, of compact alumina with different binders and at different pressures, is presented. It shows Young's modulus, the Poisson coefficient and the flexural strength. It is reported in the paper that the strength of the green ceramic bodies, created by pressure forming, is increased with the compaction pressure. This could be due to the cohesion of the granules. The effect of the binder is analyzed also in [4]. In this, only the tensile strength is found. In [5], a specimen of raw material, containing a great amount of alumina, traces of kaolin and other compounds, is studied. The mechanical properties of the green material with an organic binder were evaluated. The main conclusions are that the available, to that date, theoretical models did not describe correctly the elastic behavior of dry pressed bodies with binder. It is concluded, also, that the effect of the binder disappears after sintering. Other study of the effect of the binder can be seen in [19].

For dry pressed compacts without organic binders the same is not true. In [1] it is shown that these materials exhibit more elastic behavior. In the paper, green compacts of stoneware compositions that are used in ceramic tiles are evaluated for their mechanical properties. Different granule sizes were evaluated. Young's modulus and mechanical strength compacts made with a common slurry, used in stoneware, were found. In this paper we just evaluated green compacts that show elastic behavior.

The values for this work were obtained, by different authors, from compositions of stoneware floor tiles with no organic binder:

Table 2.1: Properties of the materials for the study

Young's modulus (E):	3.32GPa ([1])
Poisson's ratio (v):	0.3 ([2])
Bulk density (ρ):	2110 Kg/m^3 ([16])

2.2.4 Meshing

The element used for this test was the SOLID187 of ANSYS®([11]). The SOLID187 is a tetrahedral element with ten nodes and 3 degrees of freedom in each node: displacements in the X, Y and Z directions of the element.

ANSYS® SmartSize® mesher was used to generate an acceptable mesh. SmartSize®'s algorithm meshes, in this order, (i) lines, (ii) areas and (iii) volumes. This algorithm creates a very uniform mesh with very good shapes of the triangles and acceptable for solving most problems. The size level used was the finest one.

2.3 Methodology

With a few experiences, it could be said that the strength, (in the tests), of the reference tile should be higher than the strength of a tile with the same dimensions and deep back relief. The simplest way to reduce the raw material in the support is reducing the thickness of the tile. The strength of the tiles that are created with this simple method can be correctly compared. For a tile with back relief and a given volume, the strength of the tile can, also, be compared with the strength of a thin tile with the same mass. A back relief can prove that is the best both in raw material savings and strength in the given tests. Evaluating that model of back relief, with variations of its parameters, could allow the finding of a back relief that provides great savings in raw material and, at the same time, has a great strength. Following the reasoning above, the experiments are divided in two parts:

1. Compare the strength of the tiles, when there variation of the thickness of the reference tile, with the back reliefs described in section 2.2. With this method, the squares back relief was found to have the best behavior.
2. Variate the parameters that describe the tiles with squares back relief and compare their results in terms of volume and strength.

In the present work, Weibull statistics are not considered ([9]), which is the most common way to evaluate the strength of the brittle and porous materials. The evaluations, instead, are focused on the maximum first principal stresses (MFPS). The lower the maximum first principal stresses, the stronger the tile.

2.3.1 Variation of the thickness of the tile with no back relief vs tiles with back relief

The following simulations were performed. First, a set of tiles, thinner than the reference tile but with the same width and height, were modeled. A summary is shown in Table 2.2. Tests T1 and T2, as described in section 2.2, were applied and simulated. Second, the set of tiles with back relief, with their parameters shown in Table 2.3, was modeled and also made undergo tests T1 and T2.

Figs. 2.8 and 2.9 show respectively the results for test T1 and test T2. The results obtained show that, for both tests, the MFPS of each tile increases when the tile is

Table 2.2: Tiles with different thickness and without back relief, and their parameters

Model	Thickness (10^{-3}m)	Volume (10^{-4}m^3)
Reference tile	8	8.71
Thin tile #1	7	7.62
Thin tile #2	6	6.53
Thin tile #3	5	5.44
Thin tile #4	4	4.35
Thin tile #5	3	3.26

Table 2.3: Models of tiles with back relief and their parameters

Model:	Hexagons	Squares	Diamonds
Separation from border (10^{-2}m):	1	1	1
Separation between shapes (10^{-2}m):	1	1	1
Number of shapes per row:	10	10	10
Volume (10^{-4}m^3):	6.95	6.77	5.54

lighter (i.e it is less strong). As the forces acting over the tiles are mainly related to their mass, this is not completely obvious. The curves show that the MPFS of each tile is inversely proportional to the volume of the tiles lightened by making them less thick.

Given a design of deep back relief, there exists a tile with the same weight but made reducing the thickness of the reference tile. This will be called equivalent thin tile of a tile with back relief. For test T1, the values obtained for the tiles with standard squares and hexagons back reliefs lay under the curve. This means that their equivalent tiles are less strong.

A summary for the results of this test is:

1. For test T1 the squares back relief lies under the curve. The hexagons back relief also lies under the curve but is closer to it.
2. For test T1 the diamonds back relief lies over the curve and far from it.
3. For test T2 all the back reliefs lie over the curve. The diamonds back relief is far. Instead the hexagons and squares back relief are very close to the curve. The squares back relief is closer than the hexagons back relief.

Figs. 2.10 and 2.11 show, respectively, the thickest and the thinnest tiles evaluated under test T1. It is shown that the stresses of the thickest tile are not as spread as those of the thinnest tile. The thinner the model, the more spread the maximum stresses are. Figs. 2.12 and 2.13 show a very particular pattern of stresses in the back of the tile,

Figure 2.8: MFPS for the test T1. The curve represents the tiles with less thickness and the solitary points the standard back reliefs.

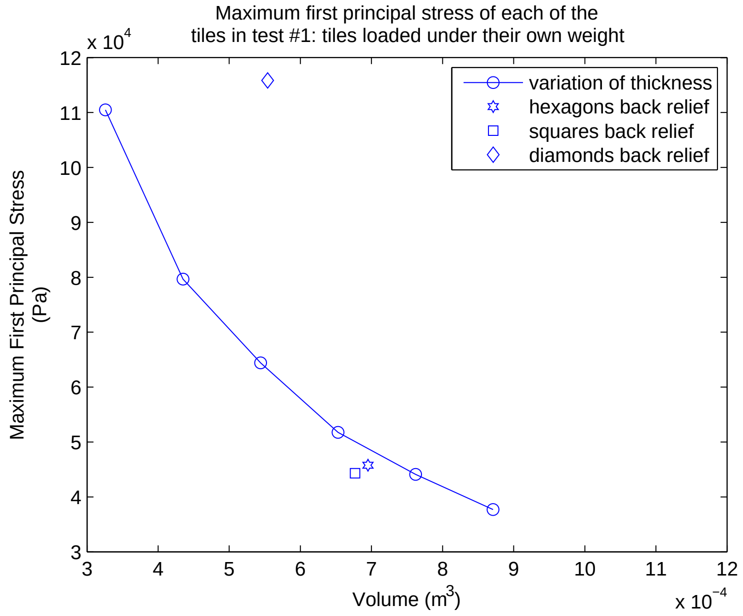

Figure 2.9: MFPS for the test T2. The curve represents the tiles with less thickness and the solitary points the standard back reliefs.

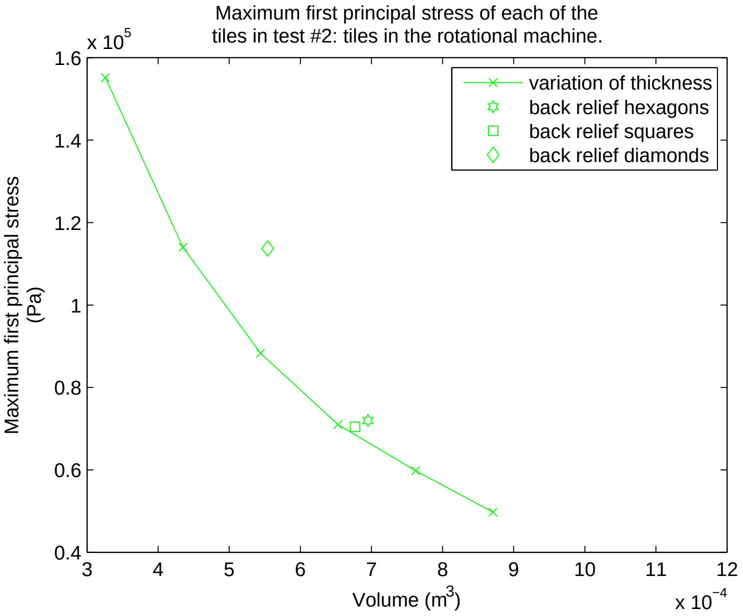

where this pattern seemed to flow horizontally. Fig. 2.14 shows the visible face of the diamonds back relief under test T2. The highest FMPS were located over the cylinder farthest from the border.

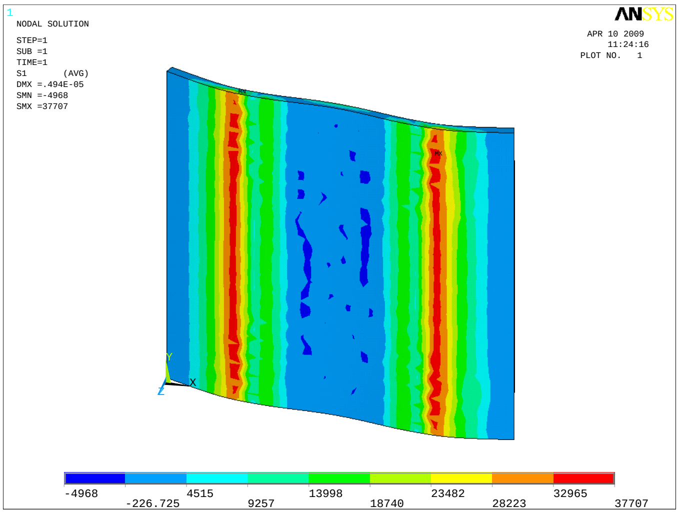

Figure 2.10: The thickest tile under test T1. The stresses are concentrated in the oposite side of the bands.

2.3.2 Parametric variations of the squares back relief

As shown in subsection 2.3.1, the back relief that had the best behavior was the squares back relief. In this subsection, that back relief will be changed in each one of its parameters to have a better understanding on how to obtain the most appropriate tile.

The following parameters were changed:

1. The depth of the prisms. The variations in the depth of the prisms and the resulting volume of each variation, are shown in table 2.4.

2. The separation between squares. The variations in separation between squares and the resulting volume of each variation, are shown in table 2.5.

3. The number of squares per row, that in this case as the tile is a square, is the same number of squares per column. The variations in the number of squares and the resulting volume for each variation are shown in table 2.6.

Figs. 2.15 and 2.16, show the effect of the variation of each one of the parameters of the squares back relief. The lines cross at the tile with default parameters for the squares back relief.

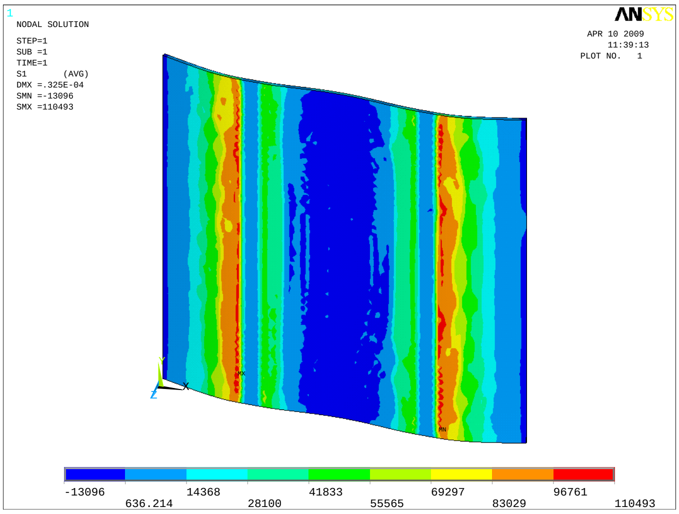

Figure 2.11: The thinnest tile under test T1. As in figure 2.10 the stresses are also concentrated in the oposite side of the bands, but are more spread.

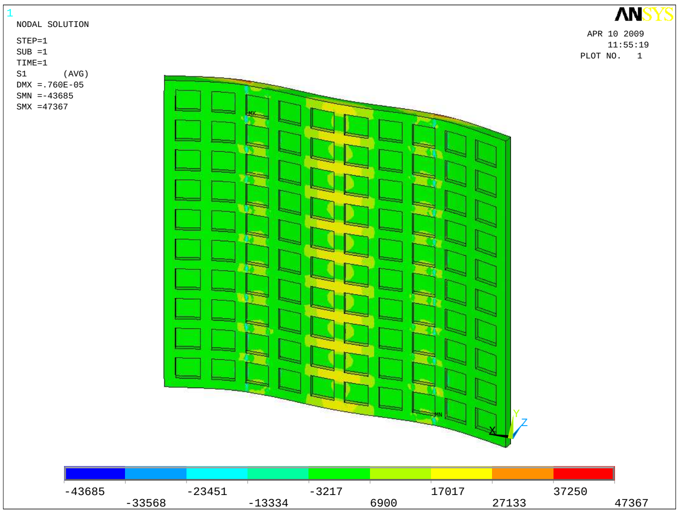

Figure 2.12: The back of the squares back relief under test T1. In the back the maximum stresses seem to flow horizontally.

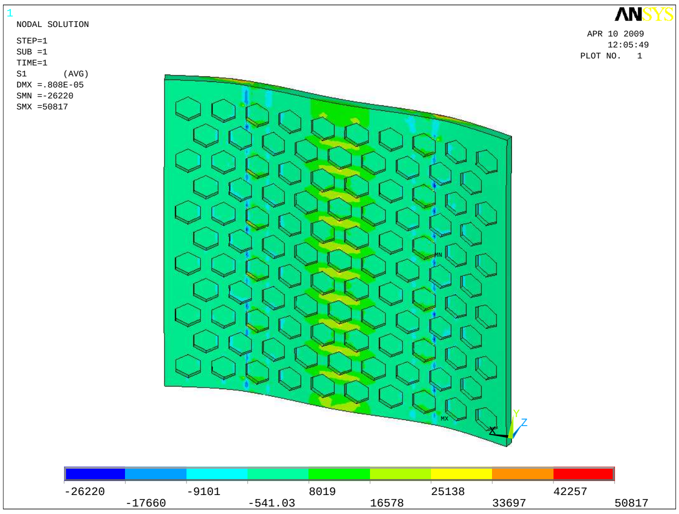

Figure 2.13: The back of the hexagons back relief under the test T1. The maximum stresses also flow horizontally, even when the areas formed by the separation between hexagons are not horizontal.

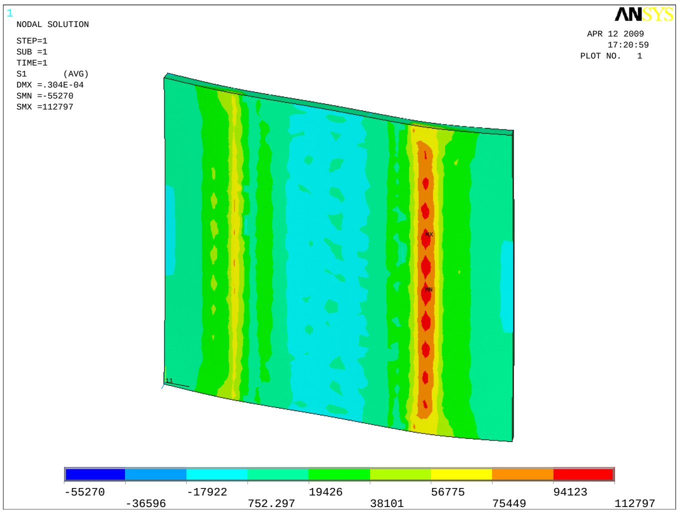

Figure 2.14: The diamonds back relief under the test T2. The maximum stresses, for all the models in this test, were concentrated near the cylinder farthest to the border.

Table 2.4: Variation in depth of the prisms subtracted from the back relief

Depth of the prisms (10^{-3}m):	1	2	3	4	5	6	7
Volume (10^{-4}m^3):	8.23	7.74	7.26	6.77	6.29	5.81	5.32

Table 2.5: Variation in separation between squares of the back relief

Separation between squares (10^{-3}m):	4	6	8	10	12	14	16
Volume (10^{-4}m^3):	5.71	6.09	6.45	6.77	7.08	7.36	7.61

Table 2.6: Variation in number of squares per row of the back relief

Number of squares per row:	4	6	8	10	12	14	16
Volume (10^{-4}m^3):	5.58	6.01	6.41	6.77	7.11	7.42	7.69

Figure 2.15: MFPS for the test T1. The curves represent each of the variations of the parameters of the squares back relief

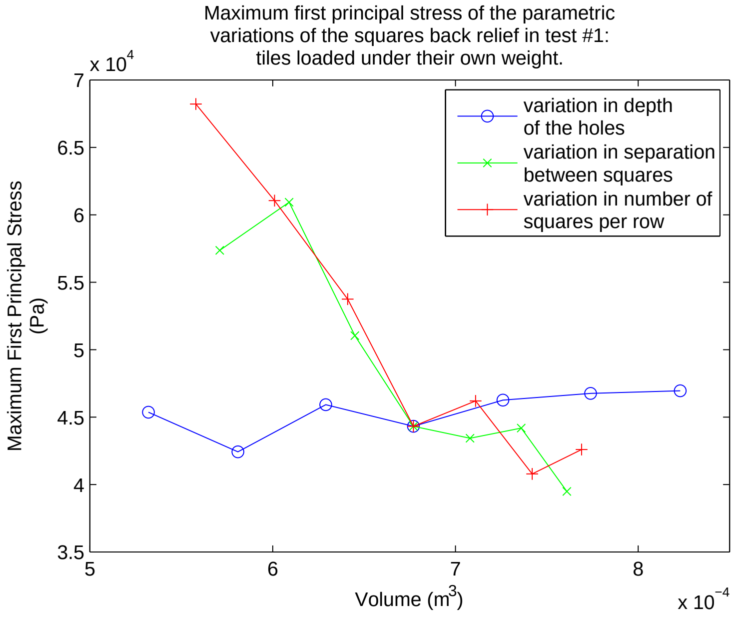

Figure 2.16: MFPS for the test T2. The curves represent each of the variations of the parameters of the squares back relief.

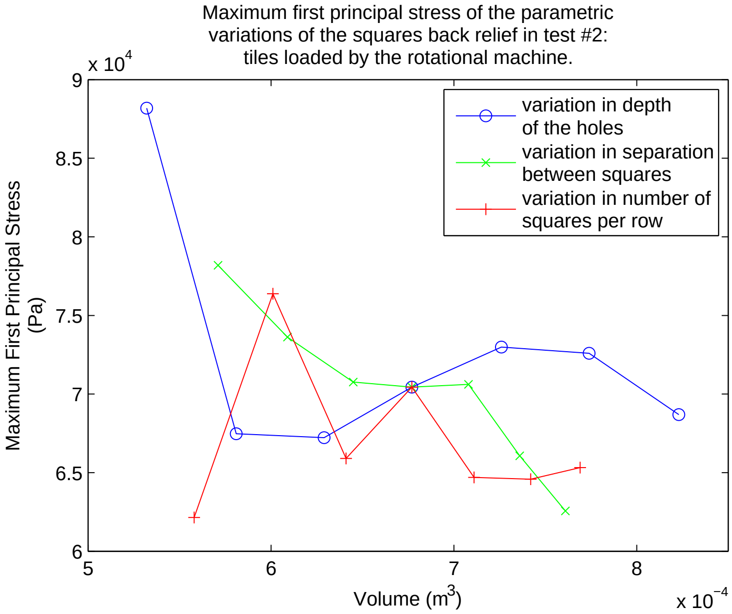

The extreme values of the variation of the back relief squares are shown in Figs. 2.17, 2.18, 2.20 and 2.19. The tile with increased depth of prisms 7mm, (Fig. 2.17), had a very good mechanical behavior and saved a lot of raw material. The tile with decreased separation between squares 4mm, (Fig. 2.18), had the worst mechanical behavior. The tile with the highest separation between squares, (Fig. 2.20) was the strongest for both test, but not the heaviest.

2.4 Conclusions and future work

This section is organized in the following form. (i) A method to evaluate the appropriateness of any model of back relief is proposed. (ii) The general conclusions of the work are presented. (iii) The future work is presented.

2.4.1 A method to evaluate the appropriateness of a model of back relief

In this paper we propose the following method. For a tile A, with back relief, and a test TX the following steps are required:

1. To calculate the volume, (V_A), and MFPS of the tile A for the test TX.

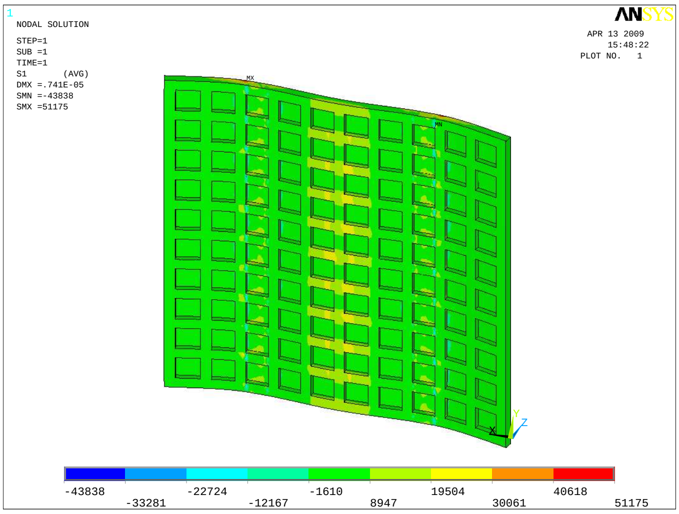

Figure 2.17: The tile evaluated that had the highest depth of the prisms subtracted under test T1. In this test, the variation of this parameter had the best behavior. Tiles with high and low depths of the prisms subtracted have almost the same strength

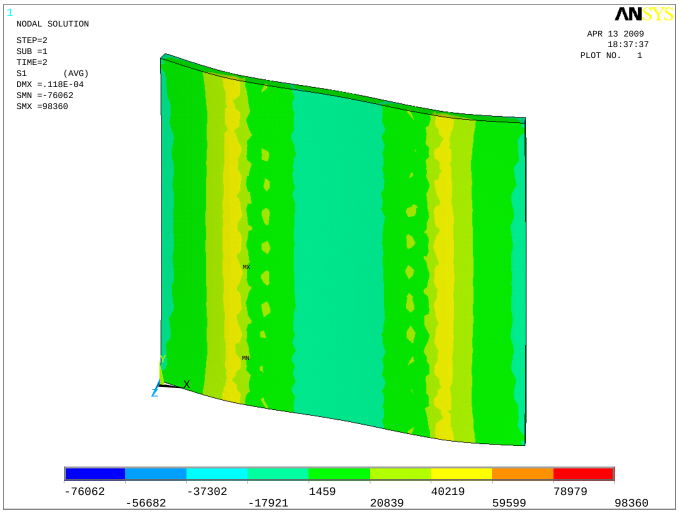

Figure 2.18: The tile evaluated that had the shortest separation between squares under test T1. In all the tests, the variation of this parameter had the worst behavior. The difference between the strengths of a tile with high and a tile with low separation between squares is considerable for both tests.

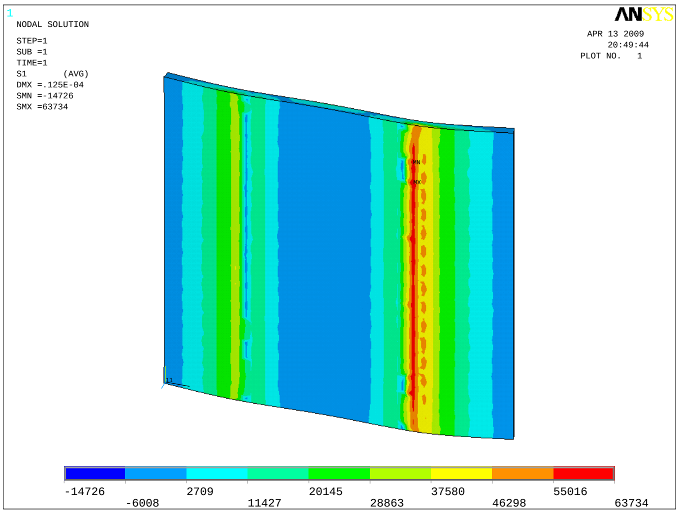

Figure 2.19: The tile evaluated that had the highest number of squares under test T2. This was one of the strongest tiles under test T2.

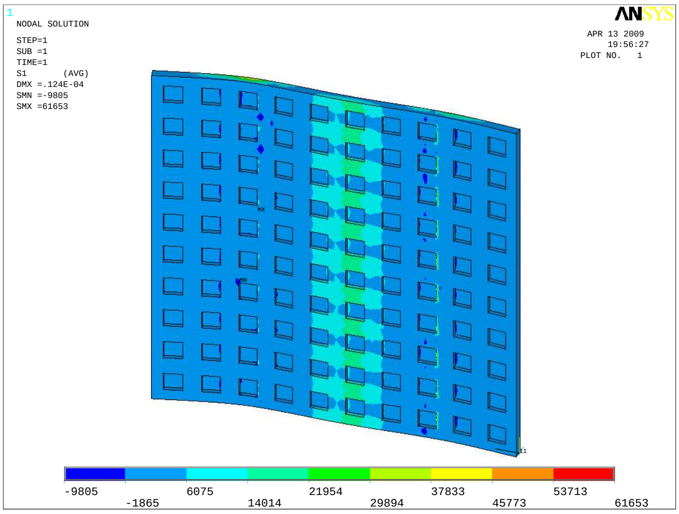

Figure 2.20: The tile evaluated that had the longest separation between squares under test T2. As mentioned in Fig. 2.17, this parameter had the worst behavior. This tile was the strongest under test T2.

2. To calculate the relative thickness, (RT_A), of a tile with the same volume, width and height but lightened by making it less thick. The formula:

   $$RT_A = \frac{V_A}{width \times height}$$

   can be used for this.

3. To calculate the MFPS of the equivalent thin tile of A, (TT_A), without back relief and with dimensions $RT_A \times width \times height$.

As shown in subsection 2.3.1 of section 2.3, this comparison would be very direct; because for both tests, the curve of the volume vs MPFS, in the case of the tiles with variation of thickness, is monotone. Instead, the curves generated by the change of the parameters of a simple back relief, like the squares back relief, were not monotone and had very strong variations.

2.4.2 General conclusions

The general conclusion is that the choice of the back relief has an important impact during the handling of the tiles in green state. Some specific conclusions can be:

1. For both tests, the MFPS that resulted from the variation of the thickness of the tiles drew a very perfect curve of the form:

   $$\text{MFPS} \propto \frac{1}{\text{VOLUME}}.$$

   This makes the thin tiles method, proposed in subsection 1 of this section, appropriate for comparing them with the tiles with deep back relief. The authors think that this will be the case for many processes that the tiles can undergo during their manufacture, even when their nature could be different.

2. The squares and the hexagons back reliefs lay under the curve, (of MFPS for reduced thickness), of test T1. That means that a tile with reduced thickness, that would have the same volume as the hexagons or squares standard back relief, would resist less than the tiles with this back relief when subject to test T1. In test T2 they both lie under the curve, but they are very close. This means that both back reliefs are appropriate for the handling in green. In both tests, the squares back relief was the best behaved. The diamonds back relief, instead, lies over both curves and very far from them. It was the worst behaved in both tests. The geometries of the squares and hexagons back reliefs are very close to each other. If we subtract their solid top, we would have connected solids that are very symmetric. In the back of the tile, the higher stresses are lines parallel

to the X axis. This is because the stresses flow between stress concentrators. In the squares back relief the stress concentrators are aligned in the same line parallel to the X axis. In the hexagons back relief the shortest paths between stress concentrators are almost parallel to the X axis, and are the places where the stresses are higher. As the hexagons back relief has more stress concentrators, it is weaker. If we subtract the solid top of the diamonds back relief, it would be disconnected. The diamonds back relief accumulates stresses near the sharp vertices of the diamonds. In these tests, specifically, this zone has higher stresses because they it supports the weight of the diamonds. This is the reason why this back relief is much weaker than the other two.

3. The variation of the parameters, chosen for the squares back relief, shown non monotonic curves that had not the same shapes for both tests. The MFPS, of a parametric variation of the squares back relief under both tests, usually decreased when the volume increased, but this was not the case for all the variations. In fact, the curves were non monotonic and searching for a minimum would require the variation of several parameters at the same time. This would be very difficult with real life experiments. Instead, computer simulations offer a very good alternative when searching the most suited deep back relief. For test T1, when the volume decreased by varying the depth of prisms; the strength did not decrease as fast as by varying the rest of the parameters. This was due to the fact that the variation in depth reduces the volume by leaving the skeleton that supports the tile unchanged. The same happened for that variation in test T2, but with a peak in the tile with less volume. For test T2 the best behavior was that of the variation of number of squares per row. Instead, for both tests, when the volume is decreased by varying the separation between the squares, the tiles become weaker with low variations in volume. This is because the sections where the stresses flow are reduced.

The general conclusion is that ceramic tiles with back relief, not only, help to increase the strength of the finished product. Depending on the design of the back relief, they can also help to reduce the waste of the tiles by increasing their strength. Computer simulations have shown to be necessary when searching for a tile that reduces the amount of raw material used and can undergo the different processes during the handling in green.

2.4.3 Future work

A lot of work has to be done to assure that the tiles with back relief can undergo the manufacturing process. Some of this work is:

1. The simulation of other stages of the ceramic tiles manufacturing process for the back relief. Important focus in the drying and dry handling, and in the sintering.
2. The evaluation, with help of the Weibull Statistics, of the probability of fracture of the compacts, could be a better measure of the strength than the MFPS.

Bibliography

[1] J.L. Amorós, V. Cantavella, J.C. Jarque, and C. Felíu. Fracture properties of spray-dried powder compacts: Effect of granule size. *Journal of the European Ceramic Society*, 28:2823–2834, 2008.

[2] J.L. Amorós, V. Cantavella, J.C. Jarque, and C. Felíu. Green strength testing of pressed compacts: An analysis of the different methods. *Journal of the European Ceramic Society*, 28:701–710, 2008.

[3] J.L. Amoros, M.J. Orts, J. Garcia-Ten, A. Gozalbo, and E. Sanchez. Effect of the green porous texture on porcelain tile properties. *Journal of the European Ceramic Society*, 27, 2007.

[4] Samir Baklouti, Thierry Chartier, and Jean François Baumard. Mechanical properties of dry-pressed ceramic green products: The effect of the binder. *Journal of the American Ceramic Society*, 80(8):1992–96, 1997.

[5] Tamara J. Carneim and David J. Green. Mechanical properties of dry-pressed alumina green bodies. *Journal of the American Ceramic Society*, 84(7):1405–10, 2001.

[6] B. Defez. Anílisis y definición del diseño óptimo del relieve al dorso en pavimentos cerámicos mediante elmentos finitos, 2007.

[7] B. Defez, G. Peris-Fajarnes, I. Tortajada, F. Brusola, and D. Larisa. Optimal design of deep back relief in ceramic floorings by means of the finite element method. *Journal of the Ceramic Society of Japan*, 116(1357):941–949, 20080901.

[8] B. Defez, G. Peris-Fajarnes, I. Tortajada, F. Brusola, and M. Samuel. Flexural strength evaluation of non-constant thickness ceramic floorings by means of the finite element method. *International Journal of Applied Ceramic Technology*, 2009.

[9] G. J. DeSalvo. Theory and structural design applications of weibull statistics, 1970.

[10] Van Vlack Lawrence H. *Physical Ceramics for Engineers*. Addison-Wesley Publishing Co., Inc., 1964.

[11] ANSYS® Inc. Theory reference for ansys® and ansys® workbench, 2003–2007.

[12] D. C. C. Lam and K. Kusakari. Microstructure and mechanical properties relations for green bodies compacted from spray dried granules. *Journal of Materials Science*, 30:5495–5501, 1995.

[13] Chris McMahon and Jimmie Browne. *CADCAM: Principles, Practice and Manufacturing Management*. Addison-Wesley Longman Publishing Co., Inc., Boston, MA, USA, 1999.

[14] S. S. Quek and G. R. Liu. *Finite Element Method: A Practical course*. Butterworth-Heinemann, 2003.

[15] David W Richerson. *Modern ceramic engineering : properties, processing and use in design*. M. Dekker, New York, N.Y, 1982.

[16] SACMI. *Tecnología cerámica aplicada*. Faenza Editrice Ibérica, 2004.

[17] Peter Stanley. Mechanical strength testing of compacted powders. *International Journal of Pharmaceutics*, 227:27–38, 2001.

[18] M. Uppalapati and D. J. Green. Effect of relative humidity on the viscoelastic and mechanical properties of spray-dried powder compacts. *Journal of the American Ceramic Society*, 89(4):1212–1217, 2006.

[19] Zhiye Zhang and David J. Green. Fracture toughness of spray-dried powder compacts. *Journal of the American Ceramic Society*, 85(5), 2002.

Conclusion

The first paper showed a new method to generate a mesh given a surface of the form $S : \mathbb{R}^2 \longrightarrow \mathbb{R}^3$. This mesh is an important step for the FEM. Of the correctness and appropriateness of this mesh depends that the solver can find a solution with a good accuracy, or even that the problem is tractable. The paper centered its attention on how to reconstruct and respect the boundaries and make them part of a triangulation that is compatible for neighbor surfaces. It showed that given certain properties of the B-rep triangulated, the triangles could be well shaped. It also showed the importance of obtaining a solution of this problem that is not heuristic.

The second paper showed step by step how to model a specific problem by means of the FEM. Defining a few parameters to generate a ceramic tile and changing them to obtain pairs of volume and strength (obtained from the Maximum First Principal Stress), served to obtain tiles better suited for this stage. The tiles with deep back relief showed to behave very well compared to the tiles lightened by reducing their thickness. It also showed that different models of deep back reliefs had a very different performance in this stage.

Appendices

Appendix A

Simulation of the Firing Ceramic Tiles

Introduction

The manufacturing of ceramic tiles is, usually, studied in an experimental manner and without the use of any computer modeling. This is because the processes involved are very complex and most of them are not well documented. Also, ceramic materials don't have simple and well described features as metals do but, as they become more important for today's technology, the nature of the processes need to be understood and also theoretical and computational models need to be developed.

The most important and studied stage of the ceramic tile manufacturing process is the firing.

In this report a research about the firing of the ceramic tiles is presented. The word sintering has the same meaning, except that is used often for very pure materials where their behavior can be understood. This report contains the following sections:

1. Theory: presents methods to transfer heat to the tiles, physical properties that are needed to describe the behavior of the tile and the stages of ceramic tiles' sintering.
2. Literature Review: presents works that have been done to simulate the sintering of ceramics specially of ceramic tiles.
3. Computational modeling: presents the steps needed to model the problem by means of the FEM, the considerations, simplifications, and the actual properties of the materials and stages of the sintering.
4. Results: presents the results obtained for the modeling. Animations that show

the curvatures, strains and temperatures are shown. Also, a discrete measure of the curvatures of the surface is presented.

A.1 Theory

The sintering transforms the raw materials from the paste into the final product giving them their finished features. The sintering works in the transmission of energy to the dry product until it reaches a established heat and during a determined time. In this way the physical and chemical reactions can be taken to the paste and the glaze so it can acquire its final properties.

The modeling of the sintering can be divided in two problems. The first involves the heat transfer from the oven to the tiles and the distribution of the heat within the ceramic body. The second involves the use of constitutive equations and possibly the shrinking of the body to calculate stresses or deformations.

The first will be called the thermal problem and the second the structural problem.

A.1.1 Thermal problem

There are several forms in which the energy can be transmitted to the tiles [1, 2, 3, 4, 5]:

1. **Conduction:** it's the least important form of heat transmission to the tiles. The heat is transmitted to the tiles by means of the bodies near them. The equation that relates the heat flow by conduction is:

$$\frac{\partial Q}{\partial t} = -k\,A\frac{\Delta T}{\Delta x} \tag{A.1.1}$$

Where $\frac{\partial Q}{\partial t}$ is the heat flow that traverses the area A in the direction x. ΔT is the difference of the temperatures between the ends located at a distance Δx. The conduction heat transfer coefficient is k.

2. **Radiation:** it's only important when the environment around the heat sinks has a great difference of temperature with them. For some works it's the most important form of heat transfer. The heat is transmitted to the tiles by electromagnetic waves that are produced with more intensity when the difference of temperatures is greater. The equation relating the rate of the heat flow (Q) transmitted between a emitter (sup) and a receiver (inf) is:

$$Q = \sigma A_{sup} F_{sup-inf}\left(T_{sup}^4 - T_{inf}^4\right) \tag{A.1.2}$$

Where A_{sup} is the area of sup that is emitting heat to inf, $F_{sup-inf}$ is the fraction of energy received by inf, (it is also called view factor, configuration factor or shape factor), σ is Stefan-Boltzmann's constant and T_{sup} and T_{inf} are the temperatures of the source and sink of heat respectively.

3. **Convection:** is the most important form of heat transfer to the tiles. The transmission of heat is carried on by the gas around the surface of the tile. The equation relating the convective heat transfer is:

$$\frac{\partial Q}{\partial t} = h\,A\,(T_{sup} - T_{inf}) \tag{A.1.3}$$

   Where $\frac{\partial Q}{\partial t}$ is the heat flow transmitted over the area A, t is the time, h is the convection heat transfer coefficient and T_{sup} and T_{inf} are the temperatures of the bulk fluid and the surface respectively.

The heat transfer in the interior of the tile can be governed by the following properties [6, 7]:

1. **Density (ρ):** it's a measure of the mass (m) per unit volume (V) of a material[6, 3, 8]. The units are reported in $\mathrm{g/cm^3}$ or in $\mathrm{Kg/m^3}$ for the MKS system. In ceramics, the term density can be used in different ways, some of them are:

   (a) Crystallographic density: the ideal density of a specific crystal structure calculated from the chemical composition and the inter-atomic spacing.

   (b) Real or theoretical density: the density of a material that contains zero microstructural porosity, i.e the mass per unit volume of the solids of the ceramic.

   (c) Bulk density: the measured density of a bulk ceramic body. It is easily obtained with the Archimedes principle: the tile is immersed in a liquid, and the volume is calculated; after that, it is weighted to measure its mass.

   (d) Specific gravity: the density of a material relative to the density of an equal volume of water at 4°C.

   The density is probably the most studied property. Studies of the density of ceramics have been related with compaction pressure and mechanical properties after sintering ([9, 10, 11, 12, 3, 13, 14, 15]) and during sintering ([16, 17, 1, 18, 19, 20, 21, 22]). Widely studied has also been the relation between density, (or porosity), with the mechanical properties, obtained analytically ([23, 24])or numerically ([25]). Density is generally the most important parameter when describing a powder compact. In the literature the density is one of the parameters that best describe the materials used for experimentation.

2. **Heat capacity (*c*):** it's the energy required to raise the temperature of a substance one degree ([6]). Its units are: J/°C. The ratio from the heat capacity of a material and the heat capacity of water, (which is about 4186 J/Kg.K), is known as the specific heat and is dimensionless. One of the major factors in the heat capacity is porosity. A ceramic material with no porosity, requires more heat energy than a porous ceramic to heat to a specific temperature.

   Few literature has been found for the heat capacity of stoneware ceramic tiles ([1, 26, 27]).

3. **Thermal conductivity (*k*):** it's the rate of heat flow through a material [6]. Its units, in SI, are: $W/\left(m \cdot K\right)$. Pure metals have a very high thermal conductivity, while organic materials have a low one. In the other side ceramics show a wide range of thermal conductivities. For a material with several phases the thermal conductivity depends on the conductivity of each of the phases and the distribution of the phases. The equations for the thermal conductivity of parallel A.1.4 and serial A.1.5 alignments resemble the ones of capacitors.

   $$k_m = V_1 k_1 + V_2 k_2 \tag{A.1.4}$$

   $$\frac{1}{k_m} = \frac{k_1 k_2}{V_1 k_2 + V_2 k_1} \tag{A.1.5}$$

   Where, k_m is the thermal conductivity of the bulk material, k_1 and V_1 are the thermal conductivity and the volume for material 1, and k_2 and V_2 are for material 2. For dispersed phases, the bulk conductivity can be approximated with equation A.1.6.

   $$k_m = k_c \left(\frac{1 + 2V_d \left(1 - k_c/k_d\right) / \left(2k_c/k_d + 1\right)}{1 - V_d \left(1 - k_c/k_d\right) / \left(k_c/k_d + 1\right)} \right) \tag{A.1.6}$$

   Where k_d and k_c are the thermal conductivities for the dispersed phase and the continuous phase respectively, and V_d is the volume fraction of the dispersed material. Porosity is a special case of dispersion, in which the dead air space, a bad conductor, is the dispersed phase.

   Few literature has been found for the thermal conductivity of stoneware ceramic tiles ([1, 26, 27]).

These properties of the material can be used to define the thermal problem as to find $T\left(x, y, z, t\right)$ where:

$$\frac{\partial T}{\partial t} = \frac{k}{\rho c} \nabla \cdot \nabla T \tag{A.1.7}$$

With boundary conditions defined by the different forms of heat transfer.

A.1.2 Structural Problem

In the structural problem the tile is expected to deform due to the uneven distribution of temperatures. Deformations are generally expressed in terms of strains (ϵ), (also called unitary deformations) . The properties that govern the deformation are:

1. **Thermal expansion:** it's the tendency of a material to change its volume when the temperature is increased or decreased. The linear thermal expansion coefficient α is calculated with the equation A.1.8:

   $$\alpha = \frac{\Delta l / l_0}{T - T_{ref}} \tag{A.1.8}$$

   Where l_0 is the length at the reference temperature T_{ref}, Δl is the change in length at T. Ceramics, (except those with cubic symmetry), have different thermal expansion along different crystallographic directions and are referred to as anisotropic or nonisotropic. If the grains in a polycrystalline ceramic have random orientation, the bulk thermal expansion of the ceramic body will be isotropic.

   If α is a function of temperature, the strains are calculated as:

   $$\epsilon = \alpha\left(T\right)\left(T - T_{ref}\right) \tag{A.1.9}$$

   At very high temperatures the change in length of a ceramic tile does not only depend on the temperature but also in the heating rate. Besides, it is not a reversible process. Linear shrinkage is then a more appropriate name for the property during sintering. It is defined as:

   $$\text{Linear shrinkage} = \Delta l / l_0 \tag{A.1.10}$$

   Linear shrinkage is a very studied property for the sintering process ([1, 28, 19, 20, 29, 30, 31, 22]). This is because it is the material property that governs the deformation of the ceramic body.

2. **Mechanical constitutive equation:** In continuum theory, constitutive equations are the way in which empirically determined material properties are expressed [32, 33]. The mechanical constitutive equation of a material relates the loads with the deformations. In the case of a linear elastic material, it is the hook law which relates the loads, (defined in terms of stresses (σ)), and the deformation, (defined in terms of strains (ϵ)):

$$\sigma = \eta\epsilon \tag{A.1.11}$$

Where η is called the elastic, (or Young's), modulus. This is the case for ceramics at ambient temperatures. Ceramic materials are anisotropic; that is, tensile stresses can produce different deformations in different dimensions. Because most of the ceramic materials are polycrystalline with random orientation of their grains, they can be threated as isotropic ([6, 7]). Stoneware ceramic tiles and other ceramic materials have been characterized in several papers with their elastic modulus ([16, 34, 35]). In certain situations in green state the tile behaves elastically ([15]). At high temperatures the elastic modulus of ceramic materials has been calculated, ([22]), but this parameter does not describe entirely the behavior of the ceramics at those temperatures.

Functions $H\left(t\right)$ and $\delta(t)$ are Heaviside step function and Dirac delta function respectively. A material is viscoelastic material if it has elastic and viscous deformations. The elastic deformation is immediate. Instead the viscous deformation also depends on time. At high temperatures ceramic materials start to describe viscoelastic behavior. Green ceramic materials have shown to be viscoelastic when they contain binders ([36, 9, 10, 11, 12, 14]).

Creep is the increase of the strain over time under a constant stress. For a constant stress ($\sigma\left(t\right) = \sigma_0$) the following equation shows the creep behavior:

$$\epsilon\left(\sigma_0, t\right) = \alpha\left(\sigma_0, t\right)\sigma_0 H\left(t\right) \tag{A.1.12}$$

Where t is the time. Instead, if a strain is given to the material and the stress is left constant, then the stresses disappear with time. This is called stress relaxation and is given by the equation:

$$\sigma\left(\epsilon_0, t\right) = \beta\left(\epsilon_0, t\right)\epsilon_0 H\left(t\right) \tag{A.1.13}$$

If $\alpha = \alpha\left(t\right)$ and $\beta = \beta\left(t\right)$, (they only depend on time) then the material is said to be linear viscoelastic. A very simple and useful model of constitutive equation for a linear viscoelastic material is Maxwell's model. Maxwell's model is a series of a linear spring and a linear dashpot. The equation for this is:

$$\frac{d\epsilon\left(t\right)}{dt}\delta(t) = \frac{d\sigma\left(t\right)}{dt}\frac{1}{\eta} + \frac{\sigma\left(t\right)}{\tilde{\eta}} \tag{A.1.14}$$

Where $\frac{\sigma}{\tilde{\eta}}$ represents the rate of strain of the damper and $\frac{d\sigma}{dt}\frac{1}{\eta}$ the rate of strain of the spring. It can be seen that $\tilde{\eta}$ is the damper coefficient and η is the elastic (or Young's) modulus. If $\sigma = \sigma_0$ the creep equation is obtained. If conversely $\epsilon = \epsilon_0$ and the differential equation that arises is solved, the stress relaxation equation can be obtained.

Ceramics at high temperatures follow a non-linear creep model. The model is described by equation:

$$\frac{d\epsilon\left(t\right)}{dt} = A{\sigma_0}^n \tag{A.1.15}$$

Where A and n are temperature dependent constants. It has also been written in the following form:

$$\frac{d\epsilon\left(t\right)}{dt} = A_0 e^{-Qc/RT}{\sigma_0}^n \tag{A.1.16}$$

Which uses an Arrhenius-like equation with $A = A_0 e^{-Qc/RT}$. T is the temperature in Kelvins, R is the ideal gas constant and Qc is the energy of activation.

When Maxwell's model (A.1.14) is combined with Norton's creep law, Norton's model is obtained:

$$\frac{d\epsilon\left(t\right)}{dt} = \frac{d\sigma\left(t\right)}{dt}\frac{1}{\eta} + A\sigma\left(t\right)^n \tag{A.1.17}$$

Where η is the elastic modulus. The main difference between equations A.1.15 and A.1.17 is that equation A.1.17 can also describe the stress relaxation phenomena. To obtain the stress relaxation equation an axial constant stress is given to a bar $(\epsilon = \epsilon_0)$. From that and equation A.1.17 the following is obtained:

$$0 = \frac{d\sigma\left(t\right)}{dt}\frac{1}{\eta} + A\sigma\left(t\right)^n \tag{A.1.18}$$

When the differential equation is solved the following is obtained:

$$\sigma\left(t\right) = \left[\left(\eta\epsilon_0\right)^{1-n} + \left(n-1\right)\eta A t\right]^{\frac{1}{1-n}} \tag{A.1.19}$$

This model needs constants η, A and n to be obtained. The creep behavior of ceramic materials at high temperatures has been extensively studied. The constant n is specially important as it can serve to describe the creep mechanism of a material ([37, 38]). It has been shown that $n \approx 1$ when the behavior is some form of diffusion creep and $3 \leq n \leq 5$ when the behavior is some kind of dislocation creep. Obtaining these parameters is very difficult ([39, 40, 41, 42, 1, 43]). It involves apparatus able to withstand very high temperatures and furnaces adapted for the task. It also involves fitting very complex functions. Those constants are dependent, not only, on the temperature but also on the heating rate, (some times also on the stress or other factors).

With these two properties the total strains are defined by:

$$\epsilon^{total} = \epsilon^{mechanical} + \epsilon^{thermal} \tag{A.1.20}$$

Where $\epsilon^{mechanical}$ is defined from equation A.1.17 and $\epsilon^{thermal}$ is defined from equation A.1.9.

A.1.3 Sintering

Some terms used in the rest of the report [3]:

1. Quartz group: is the set of diverse forms in which the silica or silicon dioxide (SiO_2) can be organized in a neutral structure.
2. Alpha Quartz (α): is the quartz referred usually. Is the most stable kind of quartz under the 573°C at $1Kbar$ of pressure. When the pressure increases this quartz becomes even more stable. Some features of this quartz are:
    (a) Crystal System: trigonal.
    (b) Specific Gravity: 2.65.
    (c) Index of Refraction: 1.55.
3. Beta Quartz (β): is the only form of quartz that is stable at more than 1300°C and pressures under $35Kbars$. The β quartz begins its transformation at 573°C. The transformation of the α quartz is quick, reversible, and is accompanied by a small amount of energy. Some properties of the β quartz are:
    (a) Crystal System: hexagonal.
    (b) Specific Gravity: 2.53.
    (c) Index of refraction: 1.54.
4. Hygroscopic water: is the water absorbed by the environment.
5. Zeolitic water: is the water that is tied to the pores since the press.

At some temperatures, during the sintering process, some critical zones can be identified. These are given, usually, to the chemical reactions of the materials during the sintering process. These zones are:

1. Under 100°C: elimination of the hygroscopic water, which the reabsorbed water from the environment during the glazing stage; or the residual humidity after a non-perfect drying.

2. Under 200°C: elimination of the zeolitic water or crystallization water. The molecules in this water are tied by absorption in the crystalline structures.
3. Between 350°C y 650°C:
   (a) Combustion of the organic substances that can be present in their different portions in the clays.
   (b) Oxidant dissociation of the oxidant sulphides with the sulfur trioxide.
4. Between 450°C y 650°C: elimination of the constitution water (dehydroxylation) and the consequent destruction of the clay's crystalline reticulum.
5. At 573°C: allotropic transformation of the quartz α in β. It generates an abrupt change in volume.
6. Between 800°C y 950°C: decarbonization of the limestone and the dolomite with the liberation of $\mathbf{CO}_2$.
7. After the 700°C: formation of new crystalline phases constituted by the $\mathbf{SiO}_2$ of the minerals.
8. After approximately 900°C: thermal dissociation of other present salts.
9. If higher temperatures are reached, some components of the pastes can be evaporated, and their coatings like the alkaline oxides, the lead oxide, the zinc oxide and the boric anhydride.

The sintering cycle

The cycle is the variation of the temperature over time. The sintering cycle is composed at least of 3 stages:

1. An increase in the temperature from the value of the environment to the maximum established and after several tests considered optimum to obtain the desired properties for the ceramic product. The velocity of the increase of the temperature is regulated in a convenient way in function of the intrinsic parameters of the material and the conditions of the work.
2. Permanence at the maximum heat of the product. This depends on the dimensions of the product and the oven. The more elevated these parameters are the demand, (for the physical and chemical transformations to be uniform), is higher.
3. Reduction of the temperature until the environment values are reached. This has to do with a program that has into account the sensitivity of the ceramic body, the heat gradient and specific demands; for example, in this stage the crystallization phenomenon will be favored, slowing down the cooling in some intervals of the temperature.

The oven

In the oven, the sintering cycle is divided in sections. In these sections the necessary machines are conditioned so, the sintering can be realized in a satisfactory way. The parts that compose the oven are:

1. Pre-oven: is the section of the oven that has the following functions:
    (a) To eliminate the hygroscopic water and the zeolitic water.
    (b) To elevate slowly the temperature of the tile.
    (c) To keep the tile at temperatures between 50 and 20°C.
    (d) To keep the gases, that are taken from other stages of the sintering, between 200 and 500°C.
2. Pre-sintering: is the section of the oven whose functions are:
    (a) To degasify the ceramic body; so, it does not have problems during the sintering.
    (b) To evaporate the rest of the zeolitic water.
    (c) To start to convert the α quartz in β quartz.
    (d) To increase in a controlled manner the temperature until the maximum; that is the temperature in which the sintering will work.

    This part of the oven has temperatures between the 500 and the 1100°. From this zone, data should be collected that will work in the sintering stage.
3. The Sintering: it is the zone of the oven where the temperature is the maximum. Its functions are:
    (a) To finish the conversion of α quartz in β quartz.
    (b) To make the chemical transformations that will give the tile finish to the tile.

    The maximum temperatures can be between the 1100 and the 1250°C.
4. Quick cooling: In this zone the tiles are cooled as fast as possible. It has the functions of:
    (a) To transform the support and the glaze state from liquid to solid.
    (b) To hold the temperature just above the re transformation of the β quartz to α quartz. The temperatures go from the sintering to the 600°C.

5. Slow cooling: is the zone where the quartz should be transformed homogeneously. Its functions are:

   (a) To change the temperature at a slow rate; such that, the tile is transformed homogeneously.
   (b) To transform, specifically, the β quartz in α quartz.

   This zone works in temperatures between the 600 and 450°C.

6. Final cooling: it is the stage dedicated to:

   (a) To reduce the temperature of the tile to the temperature of the environment as fast as possible because it has passed its critical zone.

   It is equipped with a cold air blowing system, under and over the tile.

A.2 Literature Review

Numerical simulations of the sintering can be classified according to many criteria. In the problem studied in this review there are 3 interest areas:

1. To calculate the heat transfer from an oven to a ceramic tile. That calculation includes the radiation, convection and conduction of heat to the tile to produce meaningful parameters for the control of the oven.

2. To calculate the microstructure of the ceramic component. The papers assume a geometry of the microstructure and calculate the sintering of a few particles.

3. To calculate macroscopic effects of the sintering. The macroscopic effects include deformation of the geometry and the residual stresses.

For all the interests and approaches a few examples will be shown.

There are few papers that simulate the heat transfer from the oven to the ceramic tile. In [2] the equations to simulate a single-deck roller kiln are proposed. The oven is divided into several isothermal zones and they are connected to simulate the exchange of heat between high temperature zones and low temperature ones. The number of parameters is very high and none of them are determined in the paper. In the paper the gases spent and the energy density by mass are determined for a kiln used in ceramic tiles and compared with data from the ceramic tiles industry. In [44], a ceramic oven for tiles and bricks is simulated. The most important heat transfer form is said to be the non-luminous gaseous radiation. The main goal is to obtain parameters for a controller to optimize the oven according to several parameters hierarchically organized. In [45, 46, 47, 48] descriptions of several forms to optimize the furnaces for ceramic tiles are presented. Specifically in [48], a model to estimate the distribution of temperatures in the ceramic tile is developed. The approach requires knowledge of the temperature in one of the faces of the tile, in this case the lower face that has contact with the rollers, and of the conditions within the oven. This technique is used in [1] to calculate the distribution of heat within the tile.

It has always been a top priority of the ceramic industry to obtain methods that evaluate the microstructure and final shape of the sintered bodies. For glasses, because of their amorphous nature, there are lots of methods that quantitatively evaluate at some extent these properties. For polycrystalline ceramics, instead, all the methods that are currently used are qualitative [8]. The main difficulties are:

1. Solving the equations involved: Even when the models have many simplifications, (and these simplifications are not usually approximated to the phenomena), the computational resources necessary to evaluate them are very high and the equations are dependent upon many parameters.

2. Obtaining the parameters: The constitutive equations for the model, even ignoring several conditions, have many parameters that are difficult to obtain. Many of them depend upon temperature and time and have to be evaluated at very high temperatures not suitable for usual instruments. This temperatures are, usually, near the melting point of the material.

In terms of the microstructure the sintering has 3 stages ([8]):

1. First stage (Initial Stage): A neck between adjacent particles is formed and increases until it reaches a value of $\approx 0.4-0.6$ of the particle radius. For a powder system with an initial density of $0.5 - 0.6$ of the theoretical density this corresponds to a linear shrinkage of $3-5\%$ or an increase in density to ≈ 0.65. Matter is transported by diffusion, vapor transport, plastic flow or viscous flow.

2. Second stage (Intermediate Stage): It begins when the pores have reached their equilibrium shapes as dictated by the surface and interfacial tensions. The pore phase is still continuous. Densification is assumed to occur by the pores simply shrinking to reduce their cross section. Eventually, the pores become unstable and pinch off, leaving isolated pores. This stage covers most of the sintering process and ends when the density if ≈ 0.9 of the theoretical.

3. Third stage (Final Stage): When the pores are isolated in the corners they shrink continuously and may disappear altogether. The removal of almost all the porosity has been achieved for real powder systems.

Many papers calculate the microstructure of a ceramic component. Most of them for the first stage of sintering. In [49, 50], the microstructure for a metal powder is determined and a computational model for the sintering of two particles is developed. It provides information for the final shrinkage ratio of the ceramic component which is comparable with the physical powder. Montecarlo models are the most used for this task. Papers that describe Montecarlo models for sintering include [51, 52].

When calculating macroscopic effects of the sintering, there are 3 approaches:

1. To calculate full constitutive equations using microstructural parameters as input. This requires a lot of effort in finding several microstructural parameters and fitting them. It's very difficult to even identify the constitutive equation that a powder follows.

2. To calculate some effects like deformations without using full constitutive models. This approach is championed by the use of density as a characterizing factor for all the geometrical parameters of a powder.

3. To use phenomenological relationships and calculate macroscopic parameters. After this, generally a macroscopic constitutive equation, (like Norton's model), is used.

The first approach reviewed is the one in which a full constitutive macroscopic model is obtained from a microscopic model. The parameters from the microscopic model can be obtained either numerically, analytically or phenomenologically. As sintering is a very complicated process even for a few particles, these models have only been tested with very pure ceramics for advanced components that require a lot of control in their microstructure. Some of the assumptions made include that there are no chemical reactions or that the parameters for the sintering only depend upon the density at a given time [53]. In [54, 55] the second and third stages of sintering are modeled and the deformation of a ceramic component is predicted. For the first stage of sintering a simple phenomenological model is used. In the paper several microscopic parameters are determined for a powder system, and a macroscopic constitutive model is defined. The parameters that this model requires are many, most of them obtained from phenomenological relations. Some of them are not even valid in the sintering of ceramic tiles, because of their complex nature. To solve the problem of the deformation of a component, thermal gradients and stresses due to the tools used are calculated within the program ABAQUS®, and a user routine, within this same application, is developed to obtain the sintering rates and deformations. Other papers that use the full constitutive model approach from microscopic parameters are [56, 57, 58].

There are certain simplifications that allow to formulate a numerical simulation of the sintering without using full constitutive models. In [59], a finite element method is proposed. It takes as input a set of areas that compose a planar and connected geometry of a ceramic body. Each area has a different density and all of them are fired at the same temperature and firing rate. The material property that governs the deformation in this paper is the linear shrinkage. As it has been noted, the linear shrinkage depends on the history of the temperatures that the fired body goes through. The model is valid when the history of the temperatures for the predicted deformed body is the same than the one used to evaluate the material parameters of the homogeneous specimens. It also needs to be noted that the mechanical equations are not considered in the model. The output of the algorithm is the deformed model. In [60], a densification-based finite element method is proposed. It uses the principle of the Master Sintering Curve ([53]), which states that the geometric parameters used in constitutive equations often are functions only of density. For a sintering process, in which the ceramic component has no extra forces applied, terms of the constitutive equation can be eliminated. This makes possible a formulation that depends only upon density. The paper compares the results of the simulations with other authors who simulate the sintering with full constitutive equations for very pure ceramics. It also shows that the method is applicable to a mixture of materials that resemble porcelain and obtains a good approximation. This kind of materials are certainly not suitable for simulation using a full constitutive equation. A report on this method can bee seen in [61], in which error estimation techniques are developed and more case studies are presented.

The most useful approach for the ceramic tile sintering, until now, has been to use phenomenological models that predict the macroscopic behavior without caring about the microstructure. This is because a full constitutive model has not been developed for such a complicated sintering with many phases, compounds, and with very important and highly energetic chemical reactions as the change from α-quartz to β-quartz and back to α-quartz. This is why traditionally, the process of obtaining finished traditional ceramic products has been called firing, while the term used for advanced ceramics and metals is sintering.

Constitutive models that make heavy use of phenomenological equations have been presented in many papers. For constrained sintering, in [62, 63, 64] constitutive models for solid state sintering under an applied pressure are evaluated. A stress distribution problem is reduced to an elastic one using phenomenological equations for the Young's model, and then the sintering conditions are calculated from constitutive equations. In [65], FEM is used to evaluate the sintering behavior under cold compaction. Cold compaction is a constrained sintering process in which the temperature is low, (compared to the melting point), and the creep mechanisms are despicable.

In [66], a constitutive equation in terms of macroscopic parameters is presented. These include Young's modulus, Poisson's ratio and viscosity. These parameters are calculated for an explicit rate and phenomenological equations are used so they change with the sintering conditions. The sintering of a cylinder is simulated and evaluated against an experimental specimen in terms of the shrinkage in all the directions. In [67], a phenomenological model for the sintering is developed. This admits free and constrained sintering and it's based in a Newtonian constitutive model, (linear).

There are also papers in which the densification and other sintering parameters are not modeled either phenomenologically, analytically or numerically. The parameters appearing in the equations are only determined by macroscopic experiments at different conditions that emulate the sintering. In [68] the ceramic firing process is simulated for a sample with many characteristics of that of the ceramic tile. It divides the problem into a thermal one and a structural one. The first is calculated as an isothermal one. The thermal profiles serve to calculate thermal deformation but no stresses appear. The structural problem follows a viscoelastic model. Stresses and strains appear due to the gravity.

For the best of the knowledge of the author, only two approaches have been presented to simulate the deformation of the ceramic tile during sintering. In [62, 63] the distribution of the stresses in the ceramic tile is evaluated. For this a thermal and a structural problem are defined in ANSYS®. The thermal problem uses a program of temperatures in the upper and lower faces of the tile and finds the different gradients. The structural problem uses an elastic model and finds the deformations and stresses suffered by the ceramic body. The calculations from the structural problem are fed to a model for viscous sintering to calculate the viscous deformations. In the paper only Young's modulus is found and the rest of relationships is done in base to phenomenological equations. Using the calculation of stresses in an elastic model can serve to calculate the stresses and strains in a linear viscoelastic model but not in a non-linear model as Norton's model.

In [1, 69, 70] a finite element method is developed. The heat flow is simulated in 2-dimensions, it takes into account the radiation and conduction and the heat generation, (absorption), and calculates the distribution of the temperatures in the tile. Thermal parameters k, ρ and c are calculated at different temperatures. Also the heat generation is calculated for different zones of temperature. The conduction and radiation are modeled as in [48]. For the structural problem a viscoelastic constitutive model is used. The model is a modification of Norton's model:

$$\frac{d\epsilon\left(t\right)}{dt}=\frac{d\sigma\left(t\right)}{dt}\frac{1}{\eta}+A\;e^{-b\;d\epsilon(t)/dt}\sigma\left(t\right)^{n} \tag{A.2.1}$$

The model deforms because of the thermal expansion, (or shrinkage), that the body, which is subject to different deformations, suffers. The FEM proposed is a 1-dimensional beam with different temperatures in each node. The parameters for equation A.2.1 are calculated from stress relaxation experiments at different temperatures.

This modification is made so the parameters obtained from the curves don't change with the conditions of a four-point flexural test. Small specimens of ceramic tiles are sintered to evaluate the accuracy of the method.

A.3 Computational modeling of the problem

For the finite element method, the procedure of creating a finite element model to be solved by a computer broadly consists of four steps [71]:

1. Modeling the geometry.
2. Meshing (discretization).
3. Specification of material property.
4. Specification of boundary, initial, and loading conditions.

As seen in section A.1, the problem can be divided in a thermal and a structural problem. Both of them have their own boundary conditions and material properties.

A.3.1 Modeling the geometry

A ceramic tile with deep back relief has the following geometric characteristics: (i) It's a box with 1 dimension significantly smaller than the other 2 dimensions, (ii) The thickness is non-constant; and can produce regular shapes. The other two dimensions are, usually, equal.

The ceramic tile modeled is a squared one with two sides of $33cm$ and thickness $3cm$. The tile is presented in Fig. A.1. In the figure can be seen that the sides are parallel to planes YZ and ZX respectively. The upper and lower surfaces are parallel to the plane XY. The boundary conditions that appear in the figure are explained in subsection A.3.3.

If the tile is cut in four with two planes parallel to YZ and ZX respectively and that pass by the center of the tile, it can be seen that the tile is symmetric and can be modeled as a fourth with symmetry constrains. The boundary conditions are also symmetric. The tile has been modeled as a box with two sides of $16.5mm$ and the same thicknesses. It appears in Fig. A.2.

A.3.2 Meshing (discretization)

The elements used are SOLID90 for the thermal problem and SOLID186 for the structural problem. Both are 20 node hexahedrals. The nodes at SOLID90 have one degree of freedom, the temperature. The nodes at SOLID186 have 3 degrees of freedom, displacements in X, Y and Z. SOLID186 supports, among others, large deformations and creep. The tile is meshed with ANSYS®hexahedral mesher. The mesher produces 8712 elements and 39848 nodes when 33 elements are required in the edges that serve as a border for the upper and the lower surfaces and 8 for the edges parallel to the thickness. The hexahedral mesher of ANSYS®can only be used when the geometry is a box.

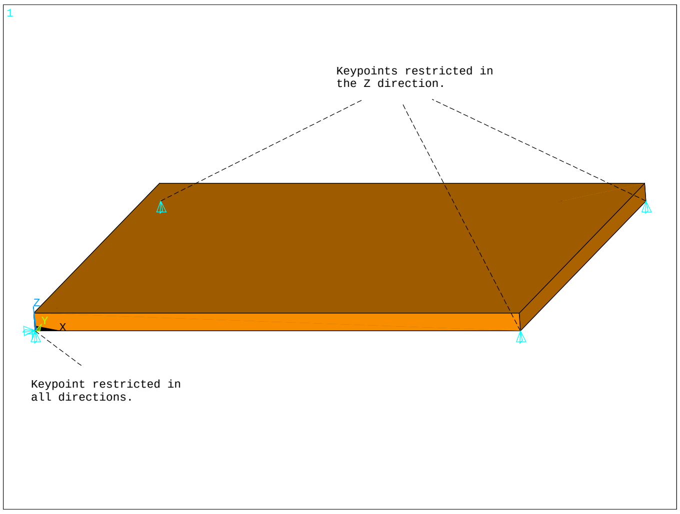

Figure A.1: Tile with displacement boundary conditions.

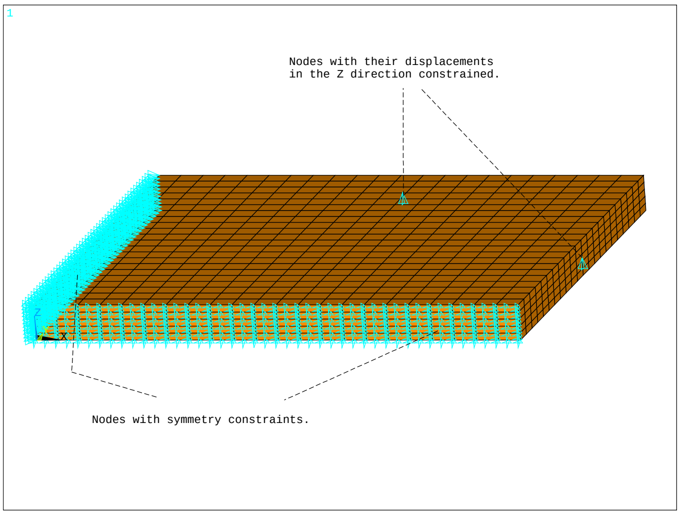

Figure A.2: Tile with symmetry boundary conditions and two nodes constrained in the Z direction.

A.3.3 Modeling the boundary conditions

The problem is modeled as follows: first a thermal simulation calculates the gradient of temperatures in function of the time. The temperatures at the nodes every certain time are applied as body force loads to an structural problem in which the deformation is calculated. The two problems are modeled as follows:

Thermal problem

A modeling of the heat transfer between the oven and the ceramic tile is a complicated one that requires very specific information about the characteristics of the oven. It has been shown that the temperatures at the lower and upper surfaces of the tile are uniform [1]. In this model constant temperatures are assigned at the surfaces. The history of temperatures is loaded from a file. The file contains the times were the temperature changes as follows:

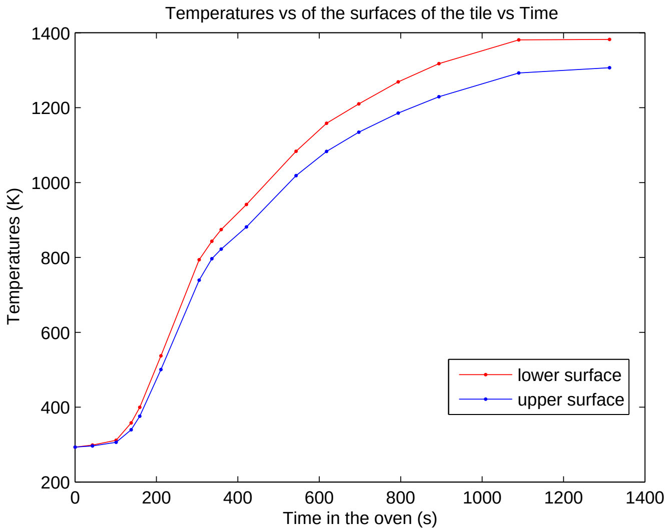

Figure A.3: Temperatures in each of the surfaces of the tile as a function of time in the oven.

At each time of the table, fixed temperatures, (Dirichlet boundary conditions), are applied at the nodes of the surfaces. The intervals between the times in the file are divided into substeps of around $5s$, (ANSYS®calculates the time so all the substeps are equal). ANSYS®makes a linear interpolation for the loads at each substep. To be able to simulate the process in the oven the temperatures at the surfaces need to be estimated.

This boundary conditions comply with the symmetry claimed in A.3.1.

A.3.4 Structural problem

The structural problem appears when the non-uniform distribution of the temperatures in the interior of the tile produces uneven deformations. This is expected to curve the tiles. The deformations occur in all directions and even the direction of the curve can change when the linear thermal expansion coefficient starts to become smaller as the temperature increases. Figure A.1 shows that three of the four lower corners have their movements restricted in the Z direction, while one of them (keypoint 4) has its movements restricted in all directions. All the movements of the tile are referenced to that keypoint. Figure A.2 shows a transformation to the problem. Symmetry constraints have been applied to the nodes in the planes YZ and ZX and two other nodes are constrained in the Z direction. These nodes constrained in the Z direction were chosen to minimize errors, this is because the constitutive model is Norton's model. In this model, $\epsilon \propto \sigma^n$. If sigma grows a little because of the errors then the strains grow much more. Errors are maximized when single nodes in corner locations are constrained. Instead, as the nodes selected in this model are not corner, the error is minimized without over constraining the model which would give a different solution that the one wanted.

The constrains, (symmetry and displacements), only serve to maintain the problem in the field of statics and ANSYS$^{®}$can calculate the equilibrium. If the simulation has no errors, no reaction forces should appear due to the constraints as all the forces are compensated internally.

A.3.5 Specifying the material properties

The material evaluated in the experiments was a common slurry used for stoneware ceramic tiles. All the properties used are taken from [1]. The chemical composition of the slurry is:

Table A.1: Properties of the materials for the study

Oxides	Mass Fraction (%)
SiO_2	63.3
Al_2O_3	17.5
Fe_2O_3	6.03
CaO	1.44
MgO	1.28
Na_2O	0.39
K_2O	3.36
TiO_2	0.79
MnO	0.04
P_2O_5	0.18

The powder is compacted to several densities. The one taken is $2\ 150\ \ \mathrm{Kg/m^3}$.

Thermal properties

Thermal properties are determined from [1]. They showed that the conduction (k) and specific heat capacity (c) did not dependent on the temperature. The properties for the thermal problem are:

Table A.2: Thermal properties of the materials for the study

Property	Value (Units)
Density (ρ)	$2\,150\ \ \mathrm{Kg/m^3}$
Thermal conductivity (k)	$0.57\ \ \mathrm{W/\,(m\,K)}$
Heat capacity (c)	$1\,250\ \ \mathrm{J/\,(Kg\,K)}$

Structural properties

Even when the behavior of the powder during firing is more complicated than a simple thermal expansion, (in which the density is only dependent on temperature), the linear coefficient of thermal expansion is used based on data collected from [1]. The secant coefficient of thermal expansion in function of the temperature is shown in Fig. A.4:

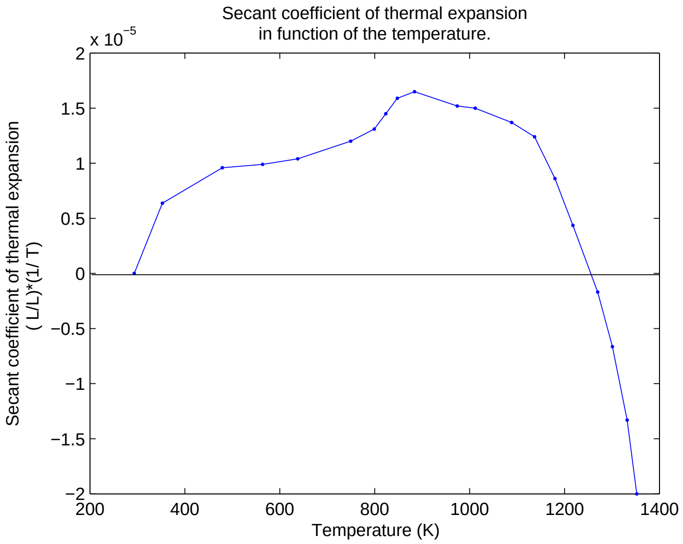

Figure A.4: Secant coefficient of thermal expansion in function of the time.

For the constitutive equations a simple Norton's model was used. The parameters that are presented in [1] can't describe a real powder. This is because the creep ratio, value that relates the creep deformation in an interval of time with the elastic deformation, was very high for temperatures under the 40°C. The test used in [1] described a relaxation test. Engauge Digitizer ([72]) is used to extract the data from the stress relaxation tests in the document. After this, a nonlinear least squares fit is used with help of equation A.1.19. The programming language R and its tools for nonlinear regression are used ([73, 74, 75, 76]).

The original mechanical properties that are found in [1] are:

Table A.3: Structural constants of the constitutive model found in [1]

T (K)	η (Pa)	A $\left(s^{-1}\right)$	n
293.15	6.5×10^{9}	1.7×10^{-17}	17
773.15	8.2×10^{9}	9.2×10^{-14}	11
973.15	9.2×10^{9}	4.3×10^{-17}	11
1073.15	11×10^{9}	4.8×10^{-13}	7
1173.15	20×10^{9}	8.0×10^{-10}	4.8
1273.15	21×10^{9}	3.8×10^{-7}	2.5
1323.15	17×10^{9}	3.2×10^{-6}	2.5
1373.15	5.7×10^{9}	3.4×10^{-5}	2.1

The properties found using R are:

Table A.4: Structural constants of the constitutive model for the study

T (K)	η (Pa)	A $\left(s^{-1}\right)$	n
293.15	3.06×10^{9}	≈ 0	-
773.15	3.75×10^{9}	2.289×10^{-26}	5
973.15	4.48×10^{9}	4.010×10^{-28}	5
1073.15	4.63×10^{9}	1.164×10^{-27}	5
1173.15	6.07×10^{9}	1.778×10^{-21}	4.27
1273.15	6.63×10^{9}	5.046×10^{-8}	2.42
1323.15	6.49×10^{9}	1.418×10^{-6}	2.30
1373.15	3.14×10^{9}	7.358×10^{-7}	2.44

It has to be recalled that there is an error when digitizing the document, but the values at 293.15 K near zero makes more sense and the values under $1\,273.15$ K show a very low creep and during the experiments this resulted in lower creep ratios. The value of 5 for n was fixed in the linear regression because ceramics have this range of creep exponents.

A.4 Results

The simulations show no convergence for the entire time in the oven. Several variations of the experiment don't give different results. However, for a range of times the simulations show convergence and are summarized in videos. Here, images of the last load step for the simulations are shown.

Fig. A.5 shows the temperature and the deformation of the tile at 655 seconds. The deformations are scaled 10 times to be able to observe the phenomenon. At certain temperatures the curvature changes of sign. This is because of the change in the sign of the slope seen in Fig. A.4.

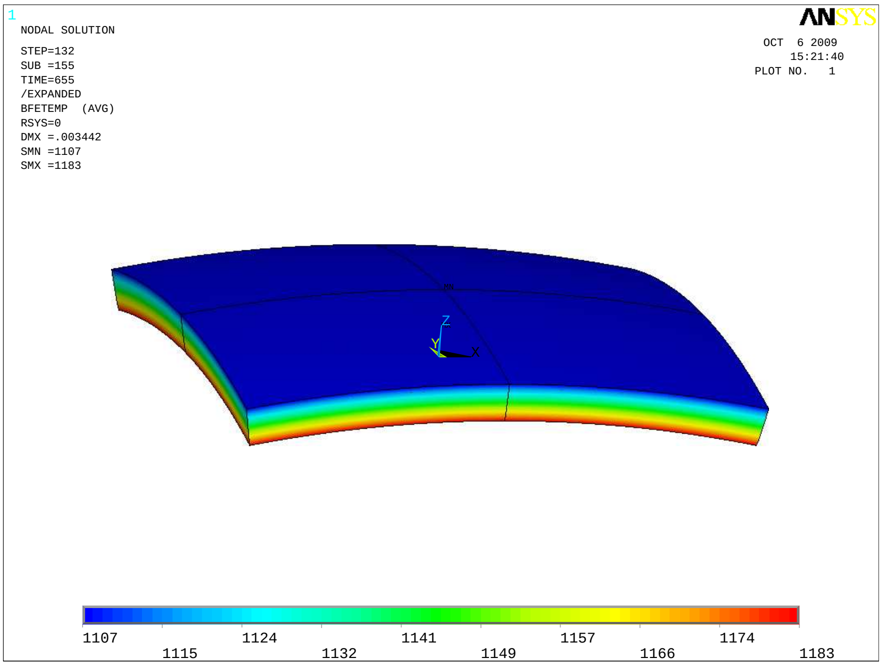

Figure A.5: Temperatures of the ceramic tile at 655 seconds.

Fig. A.6 shows the vector sum of the displacements at the last load step. Recall the constrained displacements in the Z direction for two non-corner nodes.

Fig. A.7 shows the strains, (First Principal Strains) caused by thermal expansions.

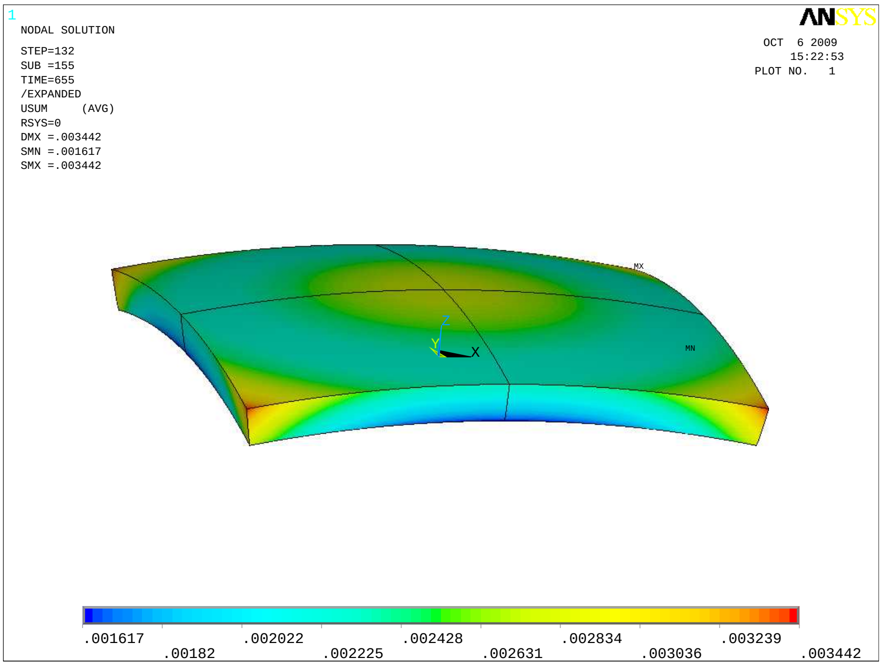

Figure A.6: Vector sum of the displacements of the ceramic tile at 655 seconds.

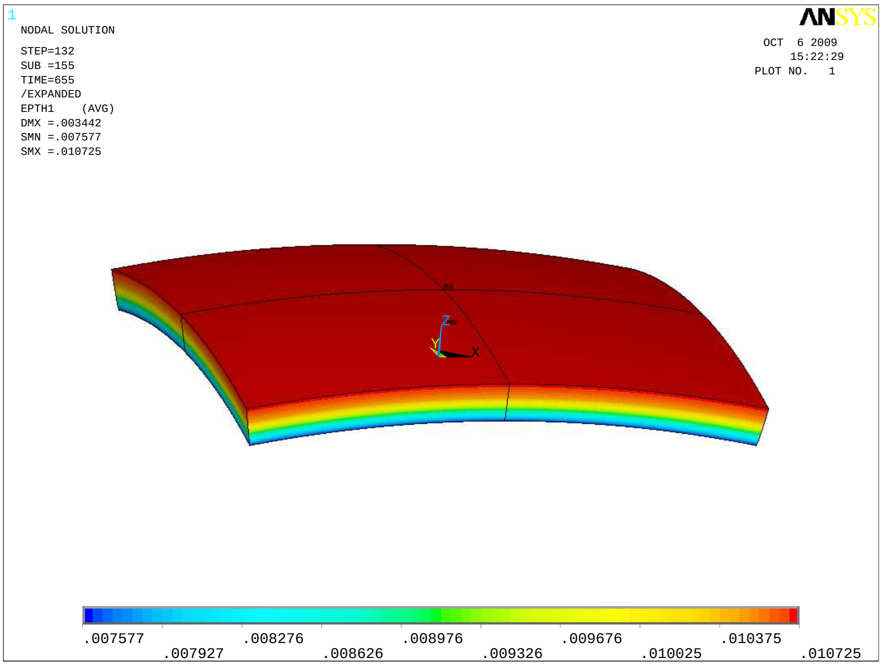

Figure A.7: First principal thermal strains of the ceramic tile at 655 seconds.

Other measures can also be captured as a function of the time but they don't show any pattern as stresses relax too quickly.

Also, a program that evaluates the mean discrete curvatures at the nodes is presented. It shows the evolution of the curvatures with the time in the oven. For this program, developed completely in ANSYS® and TCL, the mean discrete curvature is evaluated for each node using Simpson's method, ([77]). The curvatures are presented for the lower and upper surfaces of the tile.

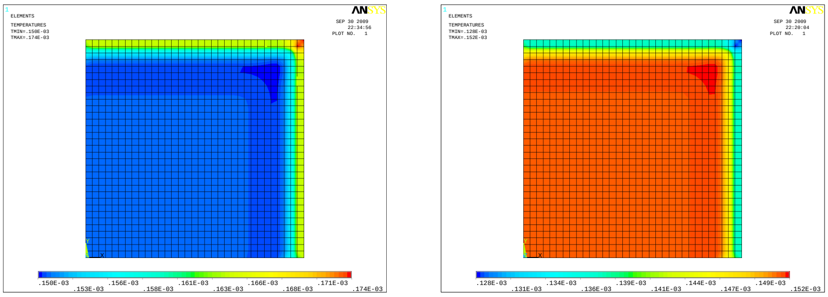

(a) Lower surface.

(b) Upper surface.

Figure A.8: Curvatures at lower and upper surfaces for time 55.

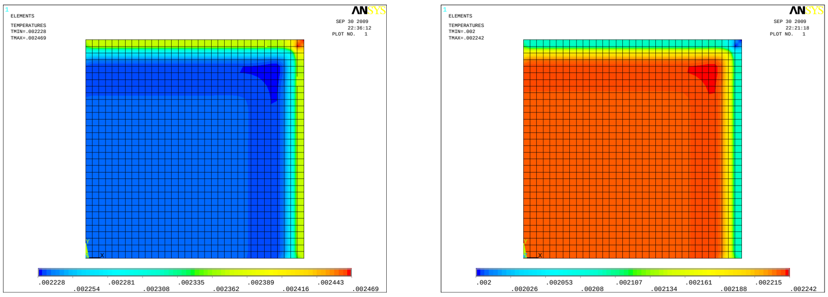

(a) Lower surface.

(b) Upper surface.

Figure A.9: Curvatures at lower and upper surfaces for time 115.

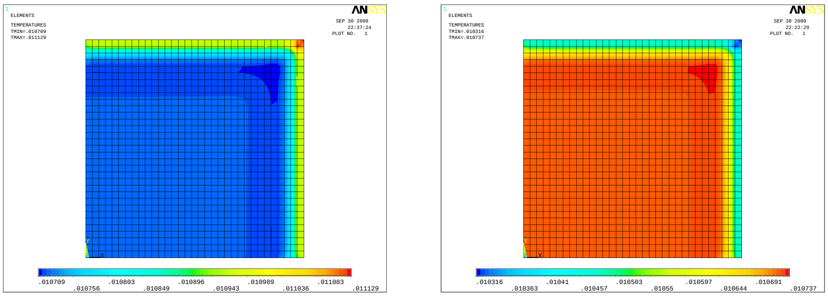

(a) Lower surface.

(b) Upper surface.

Figure A.10: Curvatures at lower and upper surfaces for time 175.

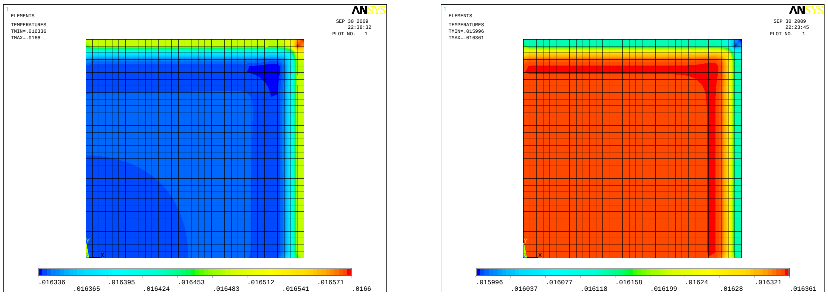

(a) Lower surface.

(b) Upper surface.

Figure A.11: Curvatures at lower and upper surfaces for time 235.

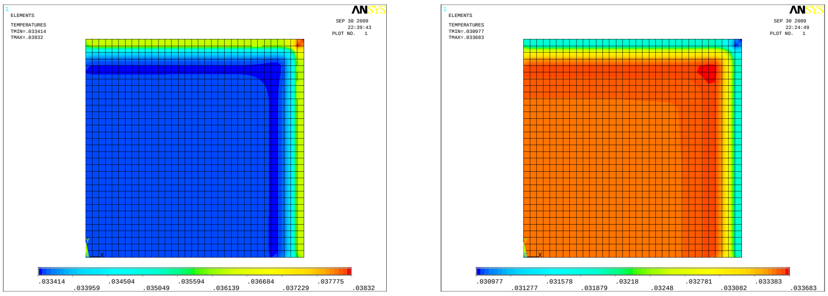

(a) Lower surface.

(b) Upper surface.

Figure A.12: Curvatures at lower and upper surfaces for time 295.

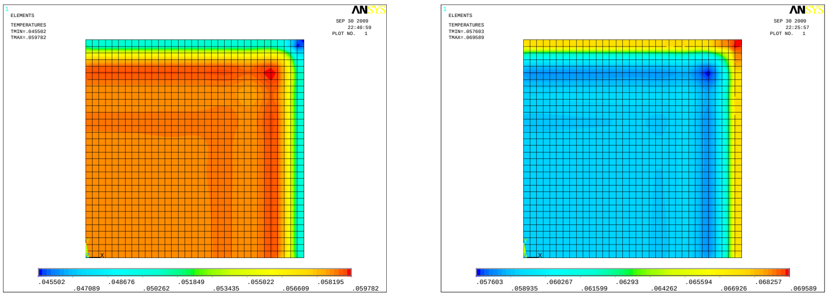

(a) Lower surface.

(b) Upper surface.

Figure A.13: Curvatures at lower and upper surfaces for time 355.

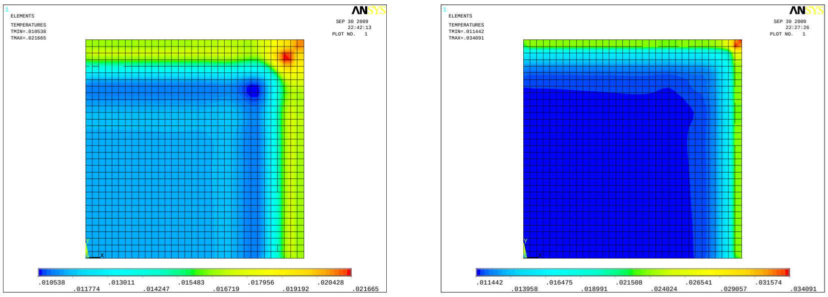

(a) Lower surface.

(b) Upper surface.

Figure A.14: Curvatures at lower and upper surfaces for time 415.

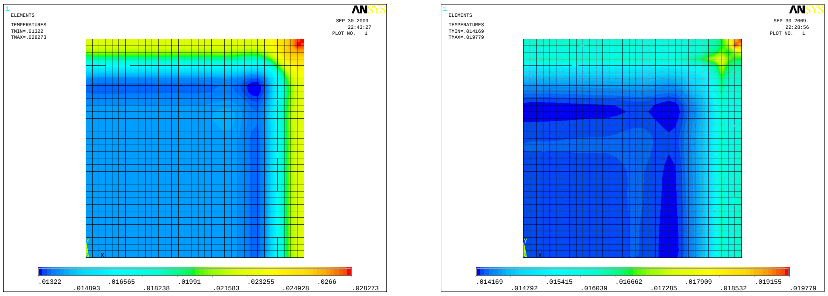

(a) Lower surface.

(b) Upper surface.

Figure A.15: Curvatures at lower and upper surfaces for time 475.

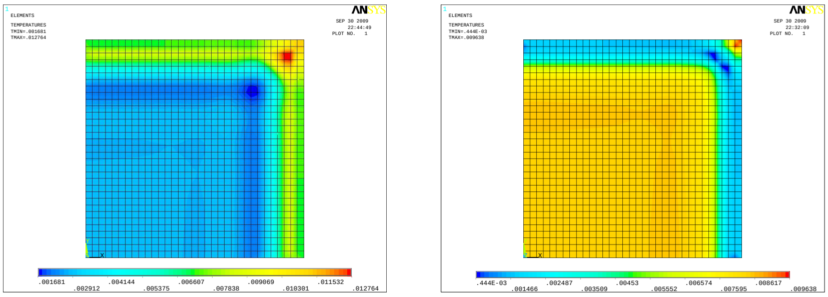

(a) Lower surface.

(b) Upper surface.

Figure A.16: Curvatures at lower and upper surfaces for time 535.

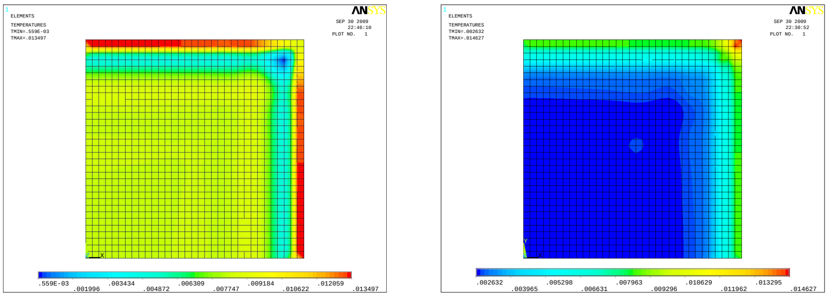

(a) Lower surface.

(b) Upper surface.

Figure A.17: Curvatures at lower and upper surfaces for time 595.

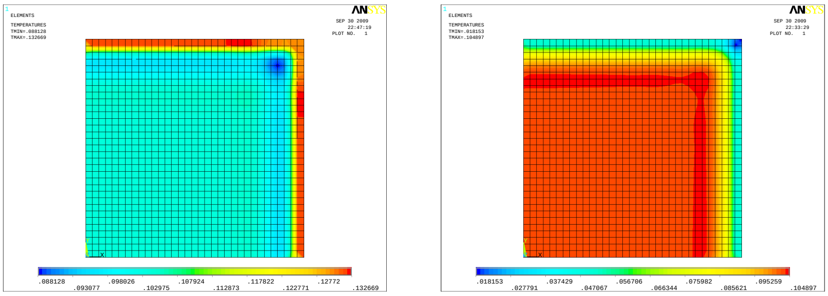

(a) Lower surface.

(b) Upper surface.

Figure A.18: Curvatures at lower and upper surfaces for time 655.

Bibliography

[1] C. Soler et al. *Simulación de la deformación de baldosas cerámicas durante la cocción*. PhD thesis, 1998.

[2] J. Uche and J.M. Marín. Simulación y optimización de un horno cerámico monocapa. *Boletín de la Sociedad Española de Cerámica y Vidrio*, 40(5):377–384, 2001.

[3] SACMI. *Tecnología cerámica aplicada*. Faenza Editrice Ibérica, 2004.

[4] A. Barba. From chemical engineering to ceramic technology: a review of research at the Instituto de Tecnología Cerámica. *Boletín de la Sociedad Española de Cerámica y Vidrio*, 44(3):155–168, 2005.

[5] V. Pitelka. *Clay: A Studio Handbook*. Amer Ceramic Society, 2001.

[6] David W Richerson. *Modern ceramic engineering : properties, processing and use in design*. M. Dekker, New York, N.Y, 1982.

[7] Van Vlack Lawrence H. *Physical Ceramics for Engineers*. Addison-Wesley Publishing Co., Inc., 1964.

[8] M.N. Rahaman. *Ceramic processing and sintering*. CRC, 2003.

[9] D. C. C. Lam and K. Kusakari. Microstructure and mechanical properties relations for green bodies compacted from spray dried granules. *Journal of Materials Science*, 30:5495–5501, 1995.

[10] Samir Baklouti, Thierry Chartier, and Jean François Baumard. Mechanical properties of dry-pressed ceramic green products: The effect of the binder. *Journal of the American Ceramic Society*, 80(8):1992–96, 1997.

[11] Tamara J. Carneim and David J. Green. Mechanical properties of dry-pressed alumina green bodies. *Journal of the American Ceramic Society*, 84(7):1405–10, 2001.

[12] Zhiye Zhang and David J. Green. Fracture toughness of spray-dried powder compacts. *Journal of the American Ceramic Society*, 85(5), 2002.

[13] S. Puchegger, F. Dose, D. Loidl, K. Kromp, R. Janssen, D. Brandhuber, N. H ”using, and H. Peterlik. The dependence of the elastic moduli of reaction bonded alumina on porosity. *Journal of the European Ceramic Society*, 27(1):35–39, 2007.

[14] J.L. Amorós, V. Cantavella, J.C. Jarque, and C. Felíu. Green strength testing of pressed compacts: An analysis of the different methods. *Journal of the European Ceramic Society*, 28:701–710, 2008.

[15] J.L. Amorós, V. Cantavella, J.C. Jarque, and C. Felíu. Fracture properties of spray-dried powder compacts: Effect of granule size. *Journal of the European Ceramic Society*, 28:2823–2834, 2008.

[16] S. Maity and BK Sarkar. Development of high-strength whiteware bodies. *Journal of the European Ceramic Society*, 16(10):1083–1088, 1996.

[17] Rajendra K. Bordia Thomas Ostrowski, Alexander Ziegler and Jurgen Rodel. Evolution of young’s modulus, strength, and microstructure during liquid-phase sintering. *Journal of the American Ceramic Society*, 81(7):1852–60, 1998.

[18] T. Ostrowski and J. Rodel. Evolution of mechanical properties of porous alumina during free sintering and hot pressing. *J. Am. Ceram. Soc.*, 82(11):3080–3086, 1999.

[19] X. Wang and P. Xiao. Characterisation of clay sintering process using impedance spectroscopy. *Journal of the European Ceramic Society*, 22(4):471–478, 2002.

[20] Giuliana Taglieri Alexander Karamanov and Mario Pelino. Sintering behavior and properties of iron-rich glass-ceramics. *Journal of the American Ceramic Society*, 87(8):1571–74, 2004.

[21] J.L. Amoros, M.J. Orts, J. Garcia-Ten, A. Gozalbo, and E. Sanchez. Effect of the green porous texture on porcelain tile properties. *Journal of the European Ceramic Society*, 27, 2007.

[22] Daniel Njopwouo Jean-Pierre Bonnet Pierre Pialy, Nicolas Tessier-Doyen. Effects of densification and mullitization on the evolution of the elastic properties of a clay-based material during firing. *Journal of the European Ceramic Society*, 2008.

[23] Gabriela Tichá Willi Pabst, Eva Gregorová. Elasticity of porous ceramics–a critical study of modulus-porosity relations. *Journal of the European Ceramic Society*, 26:1085–97, 2006.

[24] D.T. Hristopulos and M. Demertzi. A semianalytical equation for the Young's modulus of isotropic ceramic materials. *Journal of the European Ceramic Society*, 28(6):1111–1120, 2008.

[25] A.P. Roberts and E.J. Garboczi. Elastic properties of model porous ceramics. *Journal of the American Ceramic Society*, 83(12):3041–3048, 2000.

[26] A.A.R Heshmati, P. Lane, R.E. Al Gale, and AC. Janalizadeh. Numerical thermal stress analysis of ceramic tile grout removal process. 13th Association of Computational Mechanics in Engineering (ACME) Conference, 2005.

[27] I. Carmeane Effting, II Saulo G
"uths, and I. Orestes Estevam Alarcon. Evaluation of the thermal comfort of ceramic floor tiles. *Mat. Res*, 10(3), 2007.

[28] C. Leonelli, F. Bondioli, P. Veronesi, M. Romagnoli, T. Manfredini, G.C. Pellacani, and V. Cannillo. Enhancing the mechanical properties of porcelain stoneware tiles a microstructural approach. *Journal of the European Ceramic Society*, 21(6):785–793, 2001.

[29] S.J.G. Sousa and J.N.F. Holanda. Sintering behavior of porous wall tile bodies during fast single-firing process. *Materials Research*, 8:197–200, 2005.

[30] Bruno A. Latella and Tianshun Liu. High-temperature young's modulus of alumina during sintering. *Journal of the American Ceramic Society*, 88(3):773–776, 2005.

[31] J. Martín-Márquez, J.M. Rincón, and M. Romero. Effect of firing temperature on sintering of porcelain stoneware tiles. *Ceramics International*, 34(8):1867–1873, 2008.

[32] F. Irgens. *Continuum mechanics*. Springer Verlag, 2007.

[33] J. Betten. *Creep mechanics*. Springer Verlag, 2005.

[34] Frank L. Riley Cemail Aksel. Young's modulus measurements of magnesia spinel composites using load deflection curves, sonic modulus, strain gauges and rayleigh waves. *Journal of the European Ceramic Society*, 23:3089–96, 2003.

[35] CB Ustundag, YK Tur, and A. Capoglu. Mechanical behaviour of a low-clay translucent whiteware. *Journal of the European Ceramic Society*, 26(1-2):169–177, 2006.

[36] M. Uppalapati and D. J. Green. Effect of relative humidity on the viscoelastic and mechanical properties of spray-dried powder compacts. *Journal of the American Ceramic Society*, 89(4):1212–1217, 2006.

[37] W.R. Cannon and T.G. Langdon. Review: creep of ceramics, part 1: Mechanical characteristics. *J. Mater. Sci*, 18(1):1–50, 1983.

[38] W.R. Cannon and T.G. Langdon. Review: Creep of ceramics, part 2: An examination of flow mechanisms. *J. Mater. Sci.*, 23:1–20, 1988.

[39] D.K. Shetty and R.S. Gordon. Stress-relaxation technique for deformation studies in four-point bend tests: application to polycrystalline ceramics at elevated temperatures. *Journal of Materials Science*, 14(9):2163–2171, 1979.

[40] T.J. Chuang. Estimation of power-law creep parameters from bend test data. *Journal of Materials Science*, 21(1):165–175, 1986.

[41] R. Ponraj and S.R. Iyer. A simple four-point bend creep testing apparatus for brittle ceramic materials. *Journal of Materials Science Letters*, 11(14):1000–1003, 1992.

[42] R. Ponraj, S.R. Iyer, and V.M. Radhakrishnan. Creep of porcelain containing silica and alumina. *Journal of Materials Science*, 29(16):4385–4392, 1994.

[43] D.C. Cranmer and D.W. Richerson. *Mechanical testing methodology for ceramic design and reliability*. CRC Press, 1998.

[44] *Modeling and Control of Industrial Tunnel-type Furnaces for Brick and Tile Production*.

[45] A. Blasco, G. Mallol, E. Monfort, et al. Optimización de las condiciones de funcionamiento en hornos monoestrato (I). Curva de presiones. *Técnica Cerámica*, 206:585–593, 1992.

[46] JE Enrique, G. Mallol, E. Monfort, et al. Optimización de las condiciones de funcionamiento en hornos monoestrato (II). Caudal de aire de combustión. *Técnica Cerámica*, 218:716–729, 1993.

[47] G. Mallol, E. Monfort, A. Moreno, et al. Optimización de las condiciones de funcionamiento en hornos monoestrato. III Medida de gradientes transversales de temperatura. *Técnica Cerámica*, 227:653–662, 1994.

[48] J.C. Jarque, A. Moreno, J.E. Enrique, and Barba A. Optimización de las condiciones de funcionamiento en hornos monoestrato. iii medida de gradientes transversales de temperatura. *Técnica Cerámica*, 247:566–572, 1996.

[49] X. Xu, P. Lu, and R.M. German. Densification and strength evolution in solid-state sintering. Part I Experimental Investigation. *Journal of Materials Science*, 37:567–575, 2002.

[50] X. Xu, P. Lu, and R.M. German. Densification and strength evolution in solid-state sintering. Part II Strength model. *Journal of Materials Science*, 37(1):117–126, 2002.

[51] M. Braginsky, V. Tikare, and E. Olevsky. Numerical simulation of solid state sintering. *International Journal of Solids and Structures*, 42(2):621–636, 2005.

[52] E.A. Holm and C.C. Battaile. The computer simulation of microstructural evolution. *JOM Journal of the Minerals, Metals and Materials Society*, 53(9):20–23, 2001.

[53] Hunghai Su and D. Lynn Johnsonn. Master sintering curve: A practical approach to sintering. *Journal of the American Ceramic Society*, 79(12):3211–17, 1996.

[54] Hermann Riedel Torsten Kraft. Numerical simulation of solid state sintering; model and application. *Journal of the European Ceramic Society*, 24:345–361, 2004.

[55] H. Riedel and B. Blug. A comprehensive model for solid state sintering and its application to silicon carbide. *Solid Mechanics and Its Applications*, 84:49–70, 2001.

[56] E.A. Olevsky and V. Tikare. Combined macro-meso scale modeling of sintering. part i: Continuum approach. *Recent Developments in Computer Modeling of Powder Metallurgy Processes*, page 85, 2001.

[57] V. Tikare, E.A. Olevsky, and M.V. Braginsky. Combined macro-meso scale modeling of sintering. Part II, Mesoscale simulations. *Recent Developments in Computer Modeling of Powder Metallurgy Processes*, page 94, 2001.

[58] K. Shinagawa. Finite element simulation of sintering process: Microscopic modelling of powder compacts and constitutive equation for sintering. *JSME international journal. Series A, mechanics and material engineering*, 39(4):565–572, 1996.

[59] A. Easton I. Freshwater A. Tsvelikh, W. Thompson. A geometrical finite element model of the sintering process of advanced ceramics. *Computational Materials Science*, 3:457–464, 1995.

[60] Julie A. Yeomans Magali Barriere Philippe Blanchart Sasan Kiani, Jingzhe Pan. Finite element analysis of sintering deformation using densification data instead of a constitutive law. *Journal of the European Ceramic Society*, 27:2377–2383, 2007.

[61] Jingzhe Pan Ruoyu Huang. A further report on finite element analysis of sintering deformation using densification data–error estimation and constrained sintering. *Journal of the European Ceramic Society*, 28:1931–39, 2008.

[62] H. Camacho, M. E. Fuentes, L. Fuentes, A. Garcia, and Perez A. Stress distribution in ceramic tile walls under thermic dilatations. volume 42, pages 283–288. Bol. Soc. Esp. Ceram., 2003.

[63] H. Camacho, M. E. Fuentes, L. Fuentes, A. Garcia, and Perez A. Stress distribution in ceramic tile walls under thermic dilatations. volume 42, pages 353–359. Bol. Soc. Esp. Ceram., 2003.

[64] H. Camacho-Montes, P.E. Garcia-Casillas, R. Rodriguez-Ramos, M.E. Fuentes-Montero, and L.E. Fuentes-Cobas. Simulation of the stress-assisted densification behavior of a powder compact: Effect of constitutive laws. *Journal of the American Ceramic Society*, 91(3):836–845, 2008.

[65] H.G. Kim, O. Gillia, P. Dorémus, and D. Bouvard. Near net shape processing of a sintered alumina component: adjustment of pressing parameters through finite element simulation. *International Journal of Mechanical Sciences*, 44(12):2523–2539, 2002.

[66] M. Gasik and B. Zhang. A constitutive model and FE simulation for the sintering process of powder compacts. *Computational materials science*, 18(1):93–101, 2000.

[67] Didier Bouvard HongGee Kim, Olivier Gillia. A phenomenological constitutive model for the sintering of alumina powder. *Journal of the European Ceramic Society*, 23:1675–85, 2003.

[68] SH Pulko, AI Hurst, HR Newton, JM Gilbert, and AJ Wilkinson. Simulation of ceramic firing. *Computing & Control Engineering Journal*, 10(1):23–27, 1999.

[69] J. E. Enrique Navarro and Cantavella V. Model predicts tile deformation in firing. *American Ceramic Society Bulletin*, 78(10):65–69, 1999.

[70] J.E. Enrique Navarro, V. Cantavella, F. Negre, and Sanchez E. Simulation of tile deformation in firing. volume 11, page 31. Ceramica Acta., 1999.

[71] S. S. Quek and G. R. Liu. *Finite Element Method: A Practical course*. Butterworth-Heinemann, 2003.

[72] Mark Mitchell. *Engauge Digitizer*, 2009.

[73] R Development Core Team. *R: A Language and Environment for Statistical Computing*. R Foundation for Statistical Computing, Vienna, Austria, 2009. ISBN 3-900051-07-0.

[74] C. Ritz and J.C. Streibig. *Nonlinear regression with R*. Springer, 2008.

[75] SJ Sheather. *A Modern Approach to Regression with R*. Springer, New York, USA, 2009.

[76] S. Huet, A. Bouvier, M.A. Poursat, and E. Jolivet. *Statistical tools for nonlinear regression: a practical guide with S-PLUS and R examples*. Springer Verlag, 2003.

[77] Mario Botsch and Mark Pauly. Course 23: Geometric modeling based on polygonal meshes. In *ACM SIGGRAPH 2007 courses*, 2007.